The Astrophysical Journal, 856:141 (21pp), 2018 April 1 https://doi.org/10.3847/1538-4357/aaadad

The Properties of Planck Galactic Cold Clumps in the L1495 Dark Cloud

Mengyao Tang[1], Tie Liu[2,3], Sheng-Li Qin[1], Kee-Tae Kim[2], Yuefang Wu[4], Ken'ichi Tatematsu[5], Jinghua Yuan[6], Ke Wang[7], Harriet Parsons[3], Patrick M. Koch[8], Patricio Sanhueza[5], D. Ward-Thompson[9], L. Viktor Tóth[10,11], Archana Soam[2], Chang Won Lee[2,12], David Eden[13], James Di Francesco[14,15], Jonathan Rawlings[16], Mark G. Rawlings[3], Julien Montillaud[17], Chuan-Peng Zhang[17], and M. R. Cunningham[18]

[1] Department of Astronomy, Yunnan University, and Key Laboratory of Astroparticle Physics of Yunnan Province, Kunming, 650091, People's Republic of China mengyao_tang@yeah.net, slqin@bao.ac.cn
[2] Korea Astronomy and Space Science Institute, 776 Daedeokdaero, Yuseong-gu, Daejeon 34055, Republic of Korea; liu@kasi.re.kr, ktkim@kasi.re.kr
[3] East Asian Observatory, 660 N. A'ohoku Place, Hilo, HI 96720, USA
[4] Department of Astronomy, Peking University, 100871, Beijing, People's Republic of China; ywu@pku.edu.cn
[5] National Astronomical Observatory of Japan, National Institutes of Natural Sciences, 2-21-1 Osawa, Mitaka, Tokyo 181-8588, Japan
[6] National Astronomical Observatories, Chinese Academy of Sciences, Beijing, 100101, People's Republic of China
[7] European Southern Observatory, Karl-Schwarzschild-Str. 2, D-85748 Garching bei München, Germany
[8] Institute of Astronomy and Astrophysics, Academia Sinica, Taipei, Taiwan
[9] Jeremiah Horrocks Institute for Mathematics, Physics & Astronomy, University of Central Lancashire, Preston PR1 2HE, UK
[10] Eötvös Loránd University, Department of Astronomy, Pázmány Péter sétány 1/A, H-1117, Budapest, Hungary
[11] Konkoly Observatory of the Hungarian Academy of Sciences, H-1121 Budapest, Konkoly Thege Miklós út 15-17, Hungary
[12] University of Science & Technology, 176 Gajeong-dong, Yuseong-gu, Daejeon, Republic of Korea
[13] Astrophysics Research Institute, Liverpool John Moores University, IC2, Liverpool Science Park, 146 Brownlow Hill, Liverpool L3 5RF, UK
[14] NRC Herzberg Astronomy and Astrophysics, 5071 West Saanich Road, Victoria, BC V9E 2E7, Canada
[15] Department of Physics and Astronomy, University of Victoria, Victoria, BC V8P 5C2, Canada
[16] Department of Physics and Astronomy, University College London, Gower Street, London, WC1E 6BT, UK
[17] Institut UTINAM—UMR 6213—CNRS—Univ Bourgogne Franche Comte, France
[18] School of Physics, University of New South Wales, Sydney, NSW 2052, Australia
Received 2017 September 5; revised 2018 January 26; accepted 2018 February 5; published 2018 April 2

Abstract

Planck Galactic Cold Clumps (PGCCs) possibly represent the early stages of star formation. To understand better the properties of PGCCs, we studied 16 PGCCs in the L1495 cloud with molecular lines and continuum data from *Herschel*, JCMT/SCUBA-2, and the PMO 13.7 m telescope. Thirty dense cores were identified in 16 PGCCs from 2D Gaussian fitting. The dense cores have dust temperatures of $T_{\rm d}$ = 11–14 K, and H_2 column densities of N_{H_2} = (0.36–2.5) × 10^{22} cm^{-2}. We found that not all PGCCs contain prestellar objects. In general, the dense cores in PGCCs are usually at their earliest evolutionary stages. All the dense cores have non-thermal velocity dispersions larger than the thermal velocity dispersions from molecular line data, suggesting that the dense cores may be turbulence-dominated. We have calculated the virial parameter α and found that 14 of the dense cores have α <2, while 16 of the dense cores have α >2. This suggests that some of the dense cores are not bound in the absence of external pressure and magnetic fields. The column density profiles of dense cores were fitted. The sizes of the flat regions and core radii decrease with the evolution of dense cores. CO depletion was found to occur in all the dense cores, but is more significant in prestellar core candidates than in protostellar or starless cores. The protostellar cores inside the PGCCs are still at a very early evolutionary stage, sharing similar physical and chemical properties with the prestellar core candidates.

Key words: ISM: clouds – ISM: individual objects (L1495) – ISM: molecules – stars: formation

Supporting material: figure sets

1. Introduction

Stars form in dense cores within clumpy and filamentary molecular clouds (André et al. 2010). The dense cores that have no protostars are known as starless cores. When starless cores become dense enough to be gravitationally bound, they are known as prestellar cores (Ward-Thompson et al. 1994). Then, the prestellar cores collapse to form Class 0 and then Class I protostars. The prestellar cores are compact (with sizes of 0.1 pc or less), cold ($T_{\rm k} \leqslant 15$ K), and dense ($n_{H_2} > 5 \times 10^4$ cm^{-3}) starless condensations (Caselli 2011). *Herschel* observations have revealed that more than 70% of the prestellar cores (and protostars) are embedded in larger, parsec-scale filamentary structures within molecular clouds, which have column densities exceeding a minimum density threshold (~7 × 10^{21} cm^{-2}) for core formation (André et al. 2014). The properties of prestellar cores, however, are still not well known due to the lack of a large sample from observations at high spatial resolution in continuum and molecular lines. The high-frequency channels of *Planck* cover the peak thermal emission frequencies of dust colder than 14 K. A total of 13,188 Planck Galactic Cold Clumps (PGCCs) were identified (Planck Collaboration et al. 2016). PGCCs have low dust temperatures of 6–20 K, and smaller line widths, but modest column densities when compared to other kinds of star-forming clouds (Planck Collaboration et al. 2011, 2016; Wu et al. 2012; Liu et al. 2013, 2014). A large fraction of PGCCs seem to be quiescent and unaffected by ongoing star formation activity (Wu et al. 2012; Yuan et al. 2016). Those sources are the prime candidates for probing how prestellar cores form and evolve, and for studying the very early stages of star formation across a wide variety of galactic environments. A large fraction of PGCCs contain YSOs and are forming new stars. As Zahorecz

et al. (2016) pointed out based on *Herschel* data, about 25% of PGCC clumps near the Galactic mid-plane may be massive enough to form high-mass stars and star clusters. About 30% of the Taurus, Auriga, Perseus, and California PGCC clumps have associated YSOs (Tóth et al. 2016). Studying the correlation between the Planck ECC clumps (Planck Collaboration et al. 2011) and the AKARI YSOs (Tóth et al. 2014) revealed that 163 of the 915 clumps (17.8%) have at least one associated YSO within a radius equal to the semimajor axis of the clump.

The properties of the PGCCs are still not well understood due to the relatively poor resolution of the *Planck* telescope. To understand better the properties of PGCCs, we have been conducting a series of follow-up surveys toward the PGCCs with several ground-based telescopes such as the PMO (Purple Mountain Observatory) 13.7 m, the TRAO (Taeduk Radio Astronomy Observatory) 14 m, the JCMT (James Clerk Maxwell Telescope) 15 m, and the NRO (Nobeyama Radio Observatory) 45 m telescopes (Liu et al. 2012, 2013, 2014, 2016; Wu et al. 2012; Meng et al. 2013; Yuan et al. 2016; Zhang et al. 2016; Kim et al. 2017; Juvela et al. 2017; Tatematsu et al. 2017). Using the SCUBA-2 submillimeter camera on the JCMT 15 m telescope, we have been carrying out a legacy survey toward 1000 PGCCs in the 850 μm continuum, namely "SCOPE: SCUBA-2 Continuum Observations of Pre-protostellar Evolution" (Liu et al. 2018). Thousands of dense cores have been identified by the "SCOPE" survey, and most of them are either starless cores or protostellar cores with very young (Class 0/I) objects.

The L1495 cloud is located at ~140 pc (Straizys & Meistas 1980; Elias 1987; Kenyon et al. 1994; Loinard et al. 2008), and is representative of a predominantly non-clustered low-mass star formation region. Torres et al. (2012) argued that L1495 is located at a nearer distance of 131.4 pc, but here we retain a distance of 140 pc to be consistent with other studies toward L1495. The Taurus molecular cloud complex consists of clusters of cold clouds (Tóth et al. 2017), and is dominated by two roughly parallel filamentary structures, as seen, for example, in the *Herschel* Gould Belt Survey (André et al. 2010), L1495 being the most prominent filament of them. A large number of cold dense cores exist in this region (Schmalzl et al. 2010; Hacar et al. 2013; Marsh et al. 2016; Ward-Thompson et al. 2016). N_2H^+ observations toward L1495 performed by Hacar et al. (2013) suggest that at least 19 dense cores are embedded in the filamentary cloud. Other studies such as $H^{13}CO^+$ performed by Onishi et al. (2002), NH_3 by Seo et al. (2015), and continuum studies (Kirk et al. 2013; Marsh et al. 2014, 2016; Ward-Thompson et al. 2016), have suggested that L1495 cloud is composed of active low-mass star-forming regions. The properties of those dense cores in L1495, however, have not yet been fully investigated. In this paper, we aim to characterize the properties of a small sample of 16 PGCCs in the L1495 cloud, with data from *Herschel*, PMO, and SCUBA-2. The evolutionary stages, masses, density structures, and CO gas depletion of the dense cores inside the PGCCs will be investigated in detail. These studies will deepen our understandings of the physical and chemical properties of those dense cores in L1495, as well as PGCCs in general.

The paper is organized as follows. In Section 2, we present the observed data. In Section 3, we describe the observational results. In Section 4, we discuss the properties of dense cores. We summarize our findings and provide a general conclusion in Section 5.

2. Observations and Data

2.1. Herschel Data

The *Herschel Space Observatory* is a 3.5 m diameter telescope that operated in the far-infrared and submillimeter regimes (Pilbratt et al. 2010). The *Herschel* data of L1495 used in this paper are part of the *Herschel* Gould Belt Survey (André et al. 2010) and were presented by Marsh et al. (2016). The details of the observations and data reduction can be seen in André et al. (2010) and Marsh et al. (2016). In this paper, we directly used the column density and dust temperature maps of L1495 from Marsh et al. (2016), which have a 18″ angular resolution. The column density map and dust temperature map were derived from SPIRE continuum data, by fitting pixel-by-pixel SEDs using (Hildebrand 1983)

$$F_\nu = \frac{N_{\rm H_2} m_{\rm H} \mu A B_\nu(T) \kappa_\nu}{D^2}, \quad (1)$$

where F_ν is the flux density at frequency ν and B_ν is the Planck Function. $m_{\rm H}$ is the atomic hydrogen mass and μ is the mean weight of molecules taken as 2.8 (Kauffmann et al. 2008), and A is the area of each pixel. A dust mass opacity 0.144 $\rm cm^2\ g^{-1}$ has been derived for $\kappa_\nu = 0.1 \times (300/\lambda_{[\mu\rm m]})^2$ at 250 μm and a gas-to-dust mass ratio of 100 is adopted (Hildebrand 1983; Marsh et al. 2016). The pixel size is 6″. The distance D is 140 pc (Straizys & Meistas 1980; Elias 1987; Kenyon et al. 1994; Loinard et al. 2008). Therefore, only T and $N_{\rm H_2}$ are free parameters to fit. The SED fitting and maps were made by Marsh et al. (2016).

2.2. SCUBA-2 Data

The Submillimetre Common User Bolometer Array 2 (SCUBA-2) is a bolometer detector operating on the JCMT 15 m telescope with 5120 bolometers in each of two simultaneous imaging bands centred at 450 μm and 850 μm (Holland et al. 2013). In this paper we use SCUBA-2 data toward eight of the PGCCs from both the SCOPE survey (M16AL003 and M15BI061; PI: Tie Liu) and CADC[19] archival data. The archival data for G170.26-16.02 (MJLSG37) were actually taken by the SCUBA-2 Gould Belt Legacy Survey (Ward-Thompson et al. 2007; Buckle et al. 2015). The observations and programs associated with these eight PGCCs are provided in Table 1. The data were observed primarily using the CV Daisy mode. The CV Daisy is designed for small compact sources, providing a deep 3′ region in the center of the map but coverage out to beyond 12′ (Bintley et al. 2014). We used CV Daisy mode in the SCOPE survey because this mode is more efficient to quickly survey a large sample. The aim of the SCOPE survey is to detect dense condensations inside PGCCs. All the SCUBA-2 850 μm continuum data were reduced using an iterative mapmaking technique (Chapin et al. 2013; Currie et al. 2014; Mairs et al. 2015). Specifically, the data were all run with the same reduction tailored for compact sources, filtering out scales larger than 200″ on a 4″ pixel scale. A Flux Conversion Factor (FCF) of 554 Jy/pW/beam was used to convert data from pW to Jy/beam (Liu et al. 2018). The FCF in this paper is higher than the canonical value derived by Dempsey et al. (2013). This higher value reflects the impact of the data reduction technique and pixel size used by the authors. The pixel size used in the reduction of a

[19] http://www.cadc-ccda.hia-iha.nrc-cnrc.gc.ca/

Table 1
The SCUBA-2 Observations

Name	Project ID	UT	obs Number(s)	rms[a] (mJy/beam)
G168.13-16.39	M16AL003	2015 Dec 17	33	11.93
G168.72-15.48	M16AL003	2016 Jan 13	13	7.18
G169.76-16.15[b]	M16AL003	2015 Dec 27	36	12.37
G170.00-16.14[b]	M16AL003	2015 Dec 27	36	13.03
G170.26-16.02	MJLSG37[c]	2014 Nov 16	21, 25 and 24	12.50
G171.49-14.90	M16AL003	2016 Jan 17	20	9.24
G171.80-15.32	M15BI061[d]	2015 Sep 28	15	9.22
G171.91-15.65	JCMTCAL[e]	2012 Feb 11	33	8.25

Notes.
[a] The rms in the final reduced map.
[b] PGCCs G169.76-16.15 and G170.00-16.14 are covered within single observations.
[c] These observations were PONG 1800 observations observed as part of the JCMT Gould Belt Survey (Ward-Thompson et al. 2007; Buckle et al. 2015).
[d] M15BI061 is a pilot study of the SCOPE survey.
[e] JCMT calibration observation of object DGTau.

calibrator can have a significant effect on the FCF derived. The effect is different for both the beam and aperture FCFs, and also for different calibrators (Dempsey et al. 2013). Therefore, we derived a new FCF for the SCOPE survey for a default pixel size of 4″. We note that the flux calibration uncertainty in SCOPE survey is less than 10% at the 850 μm band. The archival data for G170.26-16.02 and G171.91-15.65 were calibrated with a FCF of 537 Jy/pW/beam. The FCF used for those archival data are consistent with the values (528 Jy/pW/beam for G170.26-16.02 and 526 Jy/pW/beam for G171.91-15.65) derived from the calibrators observed at the same time. We note that G170.26-16.02 was observed with Pong1800 mode. The filtering out scale for G170.26-16.02 data reduction is 600″. However, a different filtering out scale would not affect the core properties because the core sizes in G170.26-16.02 are much smaller than 100″.

2.3. PMO 13.7 m Telescope Data

Observations of the 16 PGCCs in L1495 in the ^{12}CO(1-0),^{13}CO(1-0), and C^{18}O(1-0) lines were performed with the PMO 13.7 m telescope between 2011 January and May. The 9-beam array receiver system in double-sideband (DSB) mode was used as the front end (Shan et al. 2012). The ^{12}CO(1-0) line was observed in the upper sideband and both ^{13}CO(1-0) and C^{18}O(1-0) were observed simultaneously in the lower sideband. The half-power beam width was 56″ with a main beam efficiency of 50%. The pointing and tracking accuracies were both better than 5″. The spectral resolution was ∼61 KHz, corresponding to a velocity resolution of 0.16 km s^{-1}.

The on-the-fly (OTF) observing mode was used. OTF data were converted to three-dimensional datacubes with a grid spacing of 30″. Then, we used MIRIAD (Sault et al. 1995) for further analyses. A description of the analyses of the OTF data can be found in Liu et al. (2012) and Meng et al. (2013).

3. Results

The distributions of the 16 PGCCs are shown in Figure 1, which clearly shows the filamentary structure in L1495. The names and coordinates of the 16 PGCCs are listed in Table 2.

3.1. Identification and Classification of Dense Cores

We identified dense cores within the observed PGCCs based on the column density (N_{H_2}) maps derived from *Herschel* data by eye. We did not apply any core finder algorithm because the emission peaks in the Taurus PGCCs can be very easily identified by eye. Then, the identified dense cores were fitted with a 2D Gaussian to get the physical parameters (e.g., size, temperature, density). We mainly focus on the dense cores with core-averaged column densities larger than 3×10^{21} cm^{-2}. The density threshold we used is about half of the minimum density threshold ($\sim 7 \times 10^{21}$ cm^{-2}) for core formation discovered in *Herschel* observations (André et al. 2014). Their peak column densities are also larger than $\sim 7 \times 10^{21}$ cm^{-2}. In total, the 30 most reliable dense cores with mean column densities larger than 3×10^{21} cm^{-2} are identified in 16 clumps from *Herschel* data.

As mentioned in Section 1, dense cores that have no protostars are classified as starless cores. When starless cores become dense enough to be gravitationally bound, they become prestellar cores (Ward-Thompson et al. 1994). Then, the dense cores will collapse to form Class 0 and then Class I protostars.

To investigate how core properties change with evolution, we classify the dense cores into starless, prestellar, and protostellar categories. The presence of a *Herschel* 70 μm source is a signpost of ongoing star formation (Könyves et al. 2015). Therefore, those dense cores with 70 μm emission are protostellar. In contrast, those with no 70 μm emission are starless. As an example, Figure 2 presents the *Herschel* column density map (in contours) overlaid on *Herschel* 70 μm emission map for a representative source PGCC G171.91-15.65. The cores "H1" and "H2" in G171.91-15.65 are associated with protostars, while "H3" is starless. In this paper, we only show images for G171.91-15.65. the images for other pgccs are shown in the figure set.

Prestellar cores are gravitationally bound starless cores and have higher densities than unbound starless cores. Many factors, like gravity, turbulence, magnetic field, external pressure, and even bulk motions, can affect the stability of dense cores. Therefore, it is hard to tell whether or not a starless core is gravitationally bound based on present line data. The dense starless cores detected by SCUBA-2, however, have higher densities than other starless cores (e.g., those without SCUBA-2 detection) and should be good candidates for prestellar cores (Ward-Thompson et al. 2016). Therefore, in this paper, we classify the starless cores with SCUBA-2 detection as prestellar core candidates. Hereafter, "starless cores" stand for those starless cores without SCUBA-2 detection. In total, we identify 9 protostellar cores, 6 prestellar core candidates, and 15 starless cores. The starless cores, prestellar core

Table 2
The Coordinates of Observed Planck Cold Clumps

Name	Glon (°)	Glat (°)	R.A.(J2000) (h m s)	Decl.(J2000) (d m s)	N_{VC}[a]	N_{core}[b]	$N_{condensation}$[c]
G166.99-15.34	166.99217	−15.346058	04 13 42.01	+29 44 26.31	2	1	0
G167.23-15.32	167.23387	−15.326718	04 14 30.92	+29 35 16.09	1	1	0
G168.00-15.69	168.00291	−15.694481	04 15 40.46	+28 48 00.55	1	1	0
G168.13-16.39	168.13475	−16.393131	04 13 47.56	+28 13 22.16	2	2	3
G168.72-15.48	168.72801	−15.481486	04 18 34.58	+28 26 34.64	1	2	3
G169.43-16.17	169.43114	−16.179394	04 18 23.08	+27 28 18.97	2	2	0
G169.76-16.15	169.76073	−16.159975	04 19 25.47	+27 15 16.21	2	5	3
G170.00-16.14	170.00243	−16.140558	04 20 12.04	+27 05 52.89	2	2	2
G170.13-16.06	170.13426	−16.062908	04 20 50.61	+27 03 29.08	2	1	0
G170.26-16.02	170.2661	−16.024094	04 21 21.47	+26 59 29.26	1	2	3
G170.83-15.90	170.83739	−15.907699	04 23 24.42	+26 39 55.87	2	2	0
G170.99-15.81	170.9912	−15.810754	04 24 10.41	+26 37 16.68	1	1	0
G171.49-14.90	171.49657	−14.901693	04 28 39.71	+26 51 56.81	2	1	2
G171.80-15.32	171.80418	−15.326718	04 28 07.26	+26 21 41.65	1	3	3
G171.91-15.65	171.91405	−15.655738	04 27 20.24	+26 03 50.27	1	3	2
G172.06-15.21	172.06786	−15.210718	04 29 15.63	+26 14 52.01	1	1	0

Notes.
[a] N_{VC} represents the number of velocity components.
[b] N_{core} represents the number of dense cores detected by *Herschel*.
[c] $N_{condensation}$ represents the number of dense condensations detected by SCUBA-2.

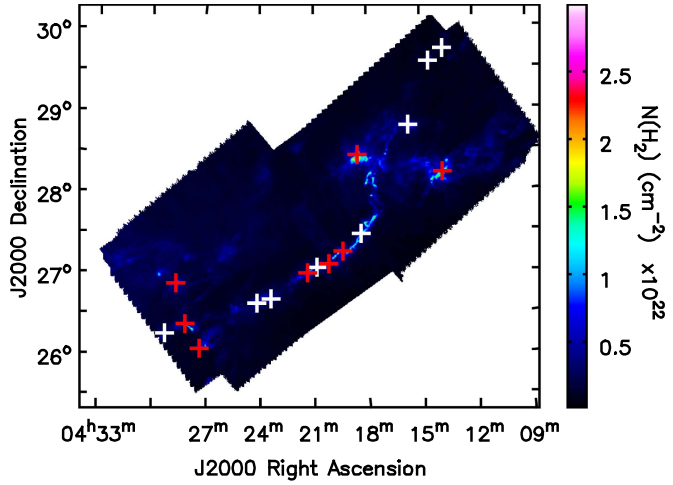

Figure 1. Spatial distribution of the observed 16 PGCCs, which are marked with crosses. The red cross represents the PGCC with SCUBA-2 detection, while the white cross represents the PGCC without SCUBA-2 detection. The color image is the *Herschel* H_2 column density map, which was derived from *Herschel* continuum data by fitting SEDs pixel-by-pixel (Marsh et al. 2016). An obvious filamentary structure in L1495 is visible.

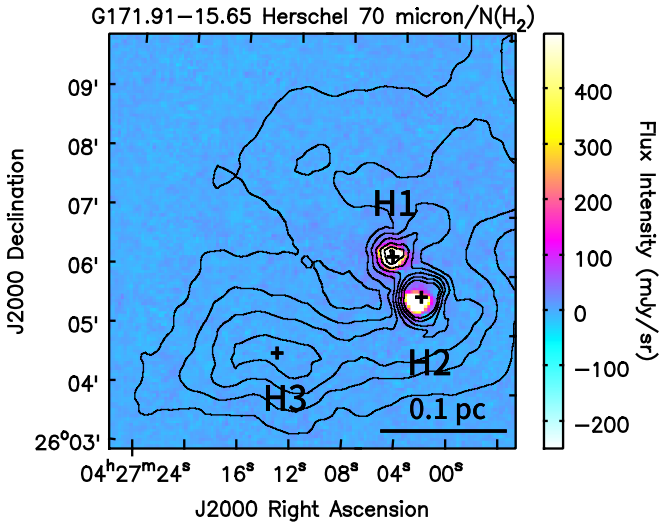

Figure 2. The *Herschel* column density map has been overlaid on a *Herschel* 70 μm continuum emission map for the representative source PGCC G171.91-15.65. The images for other sources are shown in the figure set. The contours represent the column density distribution from *Herschel*. The contour levels are from 30% to 90% of the peak value, in steps of 10%. The *Herschel* 70 μm continua are shown in color. The protostellar cores "H1" and "H2" are associated with 70 μm sources, while the starless core "H3" is not associated with any 70 μm source. The images for other sources are shown in the figure set.

(The complete figure set (8 images) is available.)

candidates, and protostellar cores are marked with 1, 2, or 3 in column 10 of Table 3, respectively.

3.2. Herschel Images

The *Herschel* column density distributions and dust temperature map are shown in contours and colors in panel (a) of Figure 3, respectively. The coordinates and FWHM deconvolved major and minor axes of the dense cores (a and b) were obtained by 2D Gaussian fits. The effective radius is $R = \sqrt{ab}\,D$, where D is the distance. The core-averaged N_{H_2}(*Herschel*) and T_d of dense cores are derived within a 2 FWHM (or 2R) area, and presented in Table 3. The core-averaged N_{H_2}(*Herschel*) of the dense cores range from $3.6(\pm1.0) \times 10^{21}$ to $2.5(\pm0.6) \times 10^{22}\,cm^{-2}$. The core-averaged dust temperatures of the dense cores range from 11.1(±0.4) to 13.8(±0.4) K. If we assume that the dense core is a sphere with a radius of R, the volume density of the core is roughly $n_{H_2} = N_{H_2}^{peak}/2R$, where $N_{H_2}^{peak}$ is the peak column density of a dense core. The volume densities (n_{H_2}) of the dense cores range from $5.7(\pm0.9) \times 10^3\,cm^{-3}$ to $7.9(\pm1.4) \times 10^4\,cm^{-3}$. The

Table 3
The Parameters Derived from *Herschel* Data

Name	Coordinate(J2000) (R.A., Decl.)	Deconvolved Size ("×")	P.A[a] (°)	N_{H_2} (Herschel) (10^{22} cm^{-2})	$N_{H_2}^{peak}$ (Herschel) (10^{22} cm^{-2})	T_d (K)	R[b] (pc)	n_{H_2} (10^4 cm^{-3})	M_{core} ($M_\odot$)	Classification[c]	Remark[d]
G166.99-15.34-H1	(4:13:41.951,+29:43:43.811)	214 × 176	−65	0.36(±0.10)	0.62	13.1(±0.4)	0.11	0.90(±0.14)	3.6(±0.6)	1	⋯
G167.23-15.32-H1	(4:14:29.120,+29:35:14.313)	233 × 112	78	0.75(±0.24)	1.19	12.5(±0.4)	0.11	1.75(±0.35)	6.7(±1.3)	1	⋯
G168.00-15.69-H1	(4:15:35.466,+28:47:23.381)	480 × 307	−86	0.59(±0.14)	0.92	12.7(±0.3)	0.26	0.57(±0.09)	29.2(±4.4)	1	⋯
G168.13-16.39-H1	(4:13:49.122,+28:12:31.360)	382 × 164	−40	1.53(±0.39)	2.54	11.9(±0.3)	0.17	2.42(±0.37)	34.6(±5.3)	3	S1
G168.13-16.39-H2	(4:14:08.510,+28:09:24.391)	627 × 164	−40	1.33(±0.14)	1.64	11.6(±0.2)	0.22	1.22(±0.11)	36.4(±3.1)	3	⋯
G168.72-15.48-H1	(4:18:33.568,+28:26:56.805)	394 × 158	−6	1.40(±0.22)	1.97	11.9(±0.3)	0.17	1.89(±0.21)	26.5(±3.0)	1	⋯
G168.72-15.48-H2	(4:18:38.298,+28:23:22.959)	251 × 169	−85	2.46(±0.60)	4.13	13.2(±1.0)	0.14	4.78(±0.70)	37.8(±5.5)	2	S1
G169.43-16.17-H1	(4:18:20.859,+27:28:27.755)	616 × 152	−43	1.05(±0.23)	1.49	11.9(±0.3)	0.21	1.16(±0.18)	30.3(±4.7)	1	⋯
G169.43-16.17-H2	(4:18:36.843,+27:22:20.914)	309 × 137	−8	0.99(±0.18)	1.35	11.8(±0.3)	0.14	1.57(±0.21)	12.3(±1.7)	1	⋯
G169.76-16.15-H1	(4:19:01.227,+27:16:50.760)	215 × 119	−27	0.97(±0.12)	1.17	11.9(±0.2)	0.11	1.74(±0.18)	6.5(±0.7)	1	⋯
G169.76-16.15-H2	(4:19:12.104,+27:13:53.438)	232 × 129	−37	0.95(±0.09)	1.09	12.2(±0.1)	0.12	1.51(±0.12)	7.1(±0.6)	1	⋯
G169.76-16.15-H3	(4:19:24.655,+27:15:05.860)	206 × 124	−48	1.05(±0.26)	1.70	12.1(±0.3)	0.11	2.53(±0.39)	9.4(±1.5)	2	S3 and 21
G169.76-16.15-H4	(4:19:37.299,+27:15:19.802)	170 × 144	−69	1.11(±0.24)	1.66	11.8(±0.3)	0.11	2.53(±0.37)	8.8(±1.3)	1	22
G169.76-16.15-H5	(4:19:42.843,+27:13:32.947)	142 × 78	−75	1.13(±0.35)	1.84	12.0(±0.3)	0.072	4.17(±0.79)	4.4(±0.8)	3	S1 and 23
G170.00-16.14-H1	(4:19:51.580,+27:11:33.739)	108 × 75	−35	1.24(±0.30)	1.82	11.1(±0.3)	0.062	4.82(±0.78)	3.2(±0.5)	2	S2 and 24
G170.00-16.14-H2	(4:19:58.119,+27:10:16.257)	144 × 79	−44	1.25(±0.42)	2.32	12.2(±0.8)	0.065	5.82(±1.05)	4.6(±0.8)	3	S1 and 25
G170.13-16.06-H1	(4:20:54.832,+27:02:42.492)	400 × 188	−89	1.16(±0.26)	1.64	11.5(±0.3)	0.19	1.43(±0.22)	26.8(±4.3)	1	30, 31 and 32
G170.26-16.02-H1	(4:21:12.207,+27:01:17.035)	101 × 50	−51	0.99(±0.17)	1.22	12.7(±0.4)	0.049	4.08(±0.56)	1.3(±0.2)	3	S2 and 34
G170.26-16.02-H2	(4:21:21.509,+26:59:53.620)	192 × 85	−52	1.24(±0.38)	2.19	11.1(±0.4)	0.087	4.08(±0.71)	7.8(±1.4)	2	S3 and 33
G170.83-15.90-H1	(4:23:37.832,+26:40:21.545)	204 × 162	48	0.53(±0.13)	0.70	12.2(±0.3)	0.12	0.93(±0.16)	5.0(±0.9)	1	⋯
G170.83-15.90-H2	(4:23:29.382,+26:38:35.041)	180 × 110	50	0.54(±0.08)	0.94	12.2(±0.3)	0.096	1.58(±0.13)	4.0(±0.4)	1	⋯
G170.99-15.81-H1	(4:24:17.134,+26:36:54.550)	669 × 308	−75	0.82(±0.18)	1.35	11.8(±0.3)	0.31	0.71(±0.10)	59.8(±8.1)	1	35 and 36
G171.49-14.90-H1	(4:28:39.189,+26:51:43.701)	135 × 92	−25	2.12(±0.67)	3.70	11.3(±0.4)	0.076	7.87(±1.43)	10.0(±1.8)	3	S1
G171.80-15.32-H1	(4:28:09.290,+26:20:44.816)	148 × 97	−60	1.50(±0.51)	2.52	11.1(±0.4)	0.082	5.01(±1.01)	7.9(±1.6)	2	S1 and 39
G171.80-15.32-H2	(4:27:54.940,+26:19:17.994)	97 × 82	70	0.89(±0.15)	1.19	12.4(±0.7)	0.061	3.17(±0.40)	2.0(±0.3)	3	S2 and 38
G171.80-15.32-H3	(4:27:48.456,+26:18:07.157)	237 × 122	59	1.34(±0.25)	1.81	11.1(±0.2)	0.12	2.54(±0.32)	11.3(±1.6)	2	S3 and 37
G171.91-15.65-H1	(4:27:04.261,+26:06:22.493)	86 × 48	36	0.78(±0.26)	1.35	13.8(±0.4)	0.044	4.99(±0.94)	1.2(±0.2)	3	S1
G171.91-15.65-H2	(4:27:02.366,+26:05:24.059)	90 × 61	30	0.98(±0.39)	2.07	13.3(±0.6)	0.051	6.63(±1.26)	2.5(±0.5)	3	S2
G171.91-15.65-H3	(4:27:13.117,+26:04:30.520)	161 × 125	−72	0.82(±0.09)	0.98	12.3(±0.1)	0.096	1.64(±0.16)	4.2(±0.4)	1	⋯
G172.06-15.21-H1	(4:29:15.723,+26:14:00.580)	215 × 113	−72	0.87(±0.26)	1.47	12.1(±0.3)	0.11	2.24(±0.40)	7.7(±1.4)	1	

Notes.
[a] Position angle of dense cores detected by *Herschel*; the convention used for measuring angles is east of north.
[b] The core radii are derived from elliptic Gaussian fitting to *Herschel* dense cores.
[c] Classification of dense cores: 1 represents a starless core, 2 represents a prestellar candidate, and 3 represents a protostellar core.
[d] S1, S2 or S3 represent the SCUBA-2 counterparts of dense cores. The numbers are source IDs of NH_3 counterparts from Seo et al. (2015).

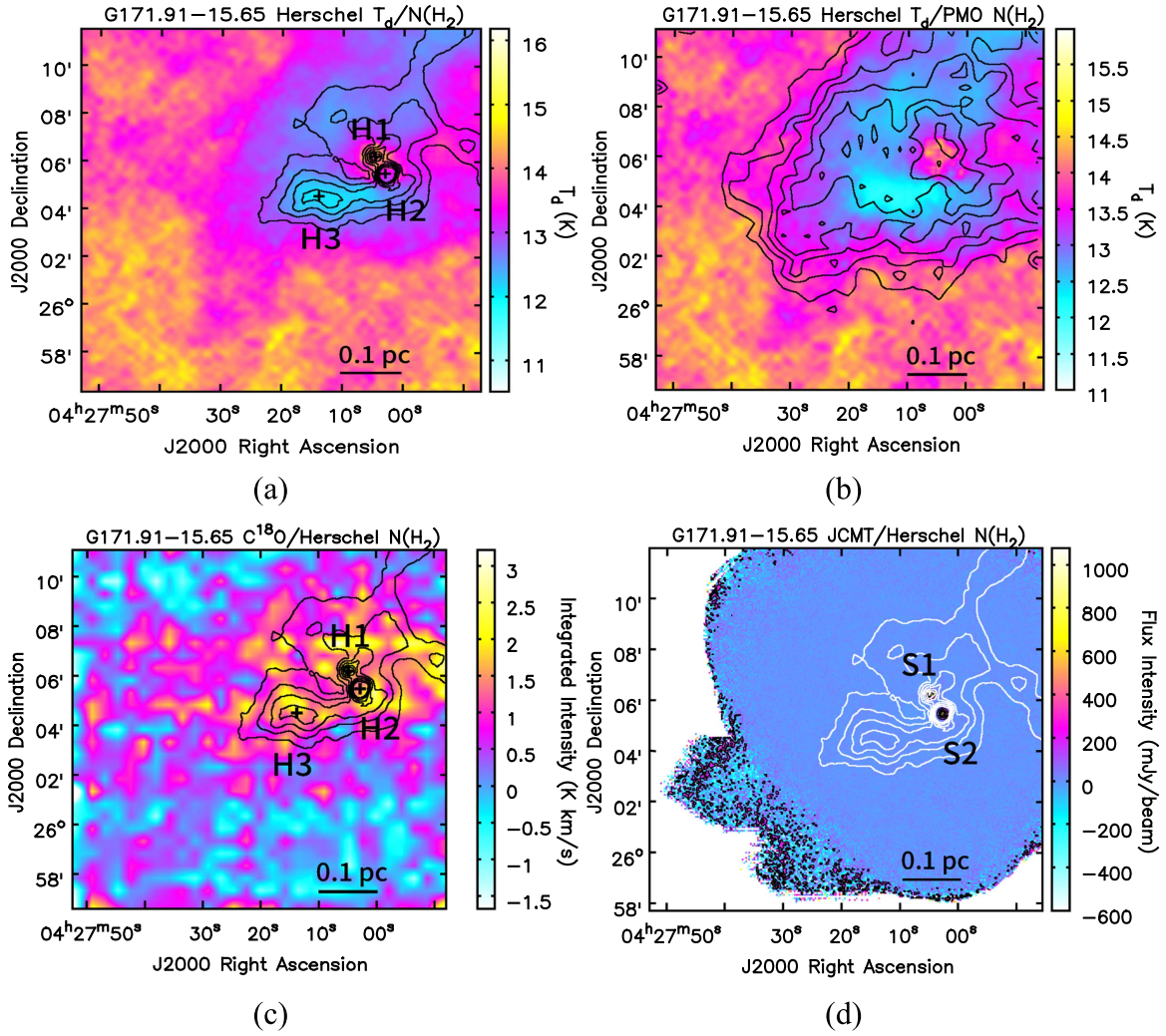

Figure 3. Panel (a): the *Herschel* column density map overlaid on the dust temperature map for the representative source PGCC G171.91-15.65. The images for other sources are shown in the figure set. The contours represent the column density distributions from *Herschel* data. The contour levels are from 30% to 90% of the peak value, in steps of 10%. Panel (b): the PMO H_2 column density map (derived from ^{13}CO data) overlaid onto the dust temperature map for the representative source PGCC G171.91-15.65. The images for other sources are shown in the figure set. The contours represent the column density distribution from PMO data. The contour levels are from 30% to 90% of the peak value, in steps of 10%. The dust temperatures are shown in color in K. Panel (c): the *Herschel* column density map overlaid onto the $C^{18}O$ integrated intensity map for the representative source PGCC G171.91-15.65. The images for other sources are shown in the figure set. The contours represent the column density distributions from *Herschel* data. The contour levels are from 30% to 90% of the peak value, in steps of 10%. The integrated intensities of $C^{18}O$ data are shown in color in K km s^{-1}. Panel (d): the *Herschel* column density map overlaid on a SCUBA-2 850 μm continuum emission map for the representative source PGCC G171.91-15.65. The images for other sources are shown in the figure set. The white contours represent the *Herschel* column density distributions. The contour levels are from 30% to 90% of the peak value, in steps of 10%. The SCUBA-2 850 μm continuum intensities are shown in color and with black contours. The contour levels are from 10 % to 90 % of the peak value, in steps of 20 %. The condensations detected by SCUBA-2 are marked with -S1, -S2 or -S3. Only two condensations are detected by SCUBA-2 in PGCC G171.91-15.65 and their sizes are smaller than the dense cores detected by *Herschel*. The images for other sources are shown in the figure set.

(The complete figure set (16 images) is available.)

masses of the dense cores are estimated as

$$M_{\rm core} = \frac{4}{3}\pi R^3 \cdot n_{\rm H_2} \cdot m_{\rm H} \cdot \mu, \quad (2)$$

where $\mu = 2.8$ is the mean molecular weight (Kauffmann et al. 2008). $m_{\rm H}$ is the mass of a H atom. The core masses $M_{\rm core}$ are presented in Table 3.

3.3. SCUBA-2 Continuum Images

Panel (d) of Figure 3 presents the 850 μm map from SCUBA-2 overlaid on a *Herschel* column density map. The SCUBA-2 detected condensations are marked with -S1, -S2, or -S3. The SCUBA-2 observations filtered out the large-scale (>200″) extended emission and only picked up the dense condensations inside the cores. Some dense cores show very flattened and extended structure, thus their emissions are mostly filtered out in SCUBA-2 observations. In total, we identified 22 condensations with signal-to-noise ratios larger than 3 from SCUBA-2 images. According to panel (d) of Figure 3, the SCUBA-2-detected condensations are consistently smaller than those detected by *Herschel*. The total integrated fluxes of these condensations were calculated from 2D Gaussian fits. The masses were consequently obtained

Table 4
Parameters of the Dense Cores Derived from SCUBA-2 850 μm Data

Name	Coordinate(J2000) (R.A., Decl.)	Total Flux (mJy)	Peak Flux Density (mJy)	Deconvolved Size ("×")	P.A[a] (°)	R(SCUBA-2)[b] (10^{-2} pc)	N_{H_2} (SCUBA-2) (10^{21} cm^{-2})	n_{H_2} (10^4 cm^{-3})	$M_{condensation}$ ($M_\odot$)	Remark[c]
G168.13-16.39-S1	(4:13:48.350,+28:12:31.114)	1096(±140)	80.40	72 × 50	20	4.10	5.63(±0.65)	2.23(±0.26)	0.44(±0.05)	H1
G168.13-16.39-S2	(4:13:54.792,+28:11:33.400)	66(±20)	71.60	14 × 14	0	0.95	5.39(±1.14)	9.20(±1.95)	0.02(±0.01)	⋯
G168.72-15.48-S1	(4:18:39.688,+28:23:24.070)	4038(±182)	183.43	89 × 51	−79	4.63	12.49(±1.27)	4.39(±0.45)	1.25(±0.13)	H2
G168.72-15.48-S2	(4:18:39.116,+28:21:56.082)	1229(±139)	75.57	116 × 37	−77	4.50	4.16(±0.44)	1.50(±0.16)	0.40(±0.04)	⋯
G168.72-15.48-S3	(4:18:03.409,+28:22:52.354)	1424(±195)	102.70	126 × 35	84	4.55	4.74(±0.59)	1.69(±0.21)	0.46(±0.06)	⋯
G169.76-16.15-S1	(4:19:42.596,+27:13:38.231)	1166(±128)	424.45	23 × 20	−74	1.48	34.88(±3.22)	38.20(±3.53)	0.40(±0.03)	H5
G169.76-16.15-S2	(4:19:41.612,+27:16:08.184)	177(±37)	144.54	14 × 14	0	0.95	12.50(±1.83)	21.36(±3.14)	0.05(±0.01)	⋯
G169.76-16.15-S3	(4:19:23.793,+27:14:54.189)	1034(±125)	76.65	84 × 37	−74	3.83	5.42(±0.60)	2.29(±0.25)	0.37(±0.04)	H3
G170.00-16.14-S1	(4:19:58.676,+27:09:58.420)	1346 ± 174)	396.04	26 × 24	58	1.74	34.05(±4.53)	31.69(±4.22)	0.48(±0.06)	H2
G170.00-16.14-S2	(4:19:51.105,+27:11:27.498)	632(±110)	81.79	59 × 41	58	3.36	4.29(±0.65)	2.07(±0.31)	0.23(±0.03)	H1
G170.26-16.02-S1	(4:21:07.522,+27:02:31.323)	257(±67)	56.54	31 × 25	−49	1.93	5.01(±1.09)	4.22(±0.92)	0.09(±0.02)	⋯
G170.26-16.02-S2	(4:21:11.866,+27:01:13.907)	578(±81)	83.59	49 × 21	−54	2.19	8.74(±1.20)	6.47(±0.88)	0.20(±0.03)	H1
G170.26-16.02-S3	(4:21:21.236,+26:59:53.873)	798(±96)	70.25	70 × 25	−54	2.91	7.03(±0.90)	3.92(±0.50)	0.28(±0.04)	H2
G171.49-14.90-S1	(4:28:39.417,+26:51:37.576)	2734(±150)	249.51	60 × 45	−13	3.56	17.00(±1.08)	7.75(±0.49)	1.01(±0.06)	H1
G171.49-14.90-S2	(4:29:04.907,+26:49:08.135)	200(±29)	170.36	14 × 14	0	0.95	14.21(±1.53)	24.28(±2.61)	0.06(±0.01)	⋯
G171.80-15.32-S1	(4:28:10.207,+26:20:28.341)	2667(±155)	186.27	91 × 61	63	5.07	7.73(±0.60)	2.47(±0.19)	0.93(±0.07)	H1
G171.80-15.32-S2	(4:27:57.598,+26:19:25.435)	1735(±169)	146.73	67 × 46	64	3.81	10.43(±1.46)	4.45(±0.62)	0.71(±0.10)	H2
G171.80-15.32-S3	(4:27:49.314,+26:18:09.353)	2871(±155)	65.58	136 × 52	63	5.76	7.15(±0.78)	2.02(±0.22)	1.11(±0.12)	H3
G171.91-15.65-S1	(4:27:04.776,+26:06:18.335)	858(±21)	88.37	14 × 14	0	0.95	67.36(±2.33)	115.07(±3.97)	0.29(±0.01)	H1
G171.91-15.65-S2	(4:27:02.654,+26:05:32.941)	1092(±8.33)	108.65	14 × 14	0	0.95	80.95(±3.23)	138.30(±5.53)	0.34(±0.01)	H2

Notes.
[a] Position angle of condensations detected by SCUBA-2; the convention used for measuring angles is east of north.
[b] The radii are derived from elliptic Gaussian fitting to SCUBA-2 condensations
[c] H1, H2, H3, or H5 represent the *Herschel* counterparts of condensations.

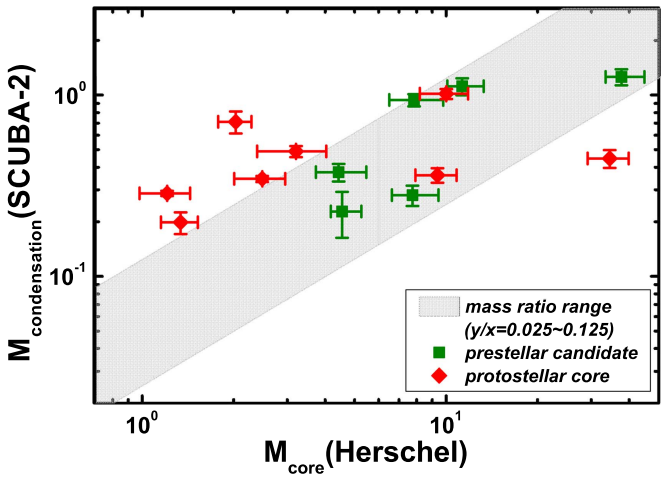

Figure 4. The correlation between $M_{\rm core}$(*Herschel*) and $M_{\rm condensation}$(SCUBA-2). The green squares and red diamonds represent prestellar candidates and protostellar cores, respectively. The gray area is the mass ratio range (0.025 ∼ 0.125). All prestellar candidates are covered by the gray area, but most protostellar cores have mass ratios higher than 0.125.

using Kauffmann et al. (2008):

$$M = 0.12\,M_\odot\,(e^{1.439(\lambda/\rm mm)^{-1}(T/10\ \rm K)^{-1}} - 1) \times \left(\frac{\kappa_\nu}{0.01\ \rm cm^2\ g^{-1}}\right)^{-1}\left(\frac{S_\nu}{\rm Jy}\right)\left(\frac{D}{100\ \rm pc}\right)^2\left(\frac{\lambda}{\rm mm}\right)^3, \quad (3)$$

where T is temperature, adopting the *Herschel* dust temperature in our calculation, D is the distance to the source, and $\kappa_\nu = 0.012$ is the dust opacity at a 850 μm wavelength, which is consistent with the value used in the SED fit to the *Herschel* data in Section 2.1. S_ν is the total flux density of the core region. The masses of the 22 SCUBA-2 condensations range from 0.02(±0.01) $M_\odot$ to 1.25(±0.13) $M_\odot$ and the column densities range from $4.2(\pm0.5)\times10^{21}\,\rm cm^{-2}$ to $8.1(\pm0.3)\times10^{22}\,\rm cm^{-2}$. The volume densities range from $1.5(\pm0.2)\times10^{4}\,\rm cm^{-3}$ to $1.4(\pm0.06)\times10^{6}\,\rm cm^{-3}$. All core parameters derived from SCUBA-2 data are presented in Table 4.

SCUBA-2 can detect condensations denser than those detected by *Herschel*. The *Herschel* volume densities of dense cores range from $5.7(\pm0.9)\times10^{3}$ to $7.9(\pm1.4)\times10^{4}\,\rm cm^{-3}$. The volume densities derived from SCUBA-2 data range from $7.4(\pm1.5)\times10^{3}$ to $9.1(\pm0.6)\times10^{5}\,\rm cm^{-3}$. The volume density estimated from the SCUBA-2 data is larger than the value estimated from the *Herschel* data, indicating that the SCUBA-2 detected condensations are denser than dense cores detected by *Herschel*. Figure 4 presents the correlation between $M_{\rm condensation}$(SCUBA-2) and $M_{\rm core}$(*Herschel*). The gray area represents mass ratios that range from 0.025 to 0.125. The green squares and red diamonds represent prestellar candidates and protostellar cores, respectively. All prestellar candidates in Figure 4 are covered by a gray area, but most protostellar cores have mass ratios higher than 0.125. This indicates that protostellar cores are generally more concentrated than prestellar candidates. This may indicate that as cores evolve, the volume density distributions of dense cores will be more centrally concentrated.

Ward-Thompson et al. (2016) identified 25 dense condensations in the L1495 cloud based on SCUBA-2 observations. According to their results, the mass of dense condensations ranges from 0.02 to 0.61 $M_\odot$, with a mean value of 0.19. Their radii range from 0.02 to 0.03 pc, with a mean value of 0.03 pc. It should be noted that they have taken β as 1.3 to the derived κ_ν in their calculations. If $\beta = 2$ were taken, their condensations' masses would be doubled and be very similar to our SCUBA-2-detected condensations in PGCCs (mass ranging from 0.02 to 1.25 $M_\odot$, with a mean value of 0.45 $M_\odot$, and radii ranging from 0.02 to 0.06 pc, with a mean value of 0.03 pc.)

3.4. Results of PMO Molecular Lines

The ^{12}CO(1-0), ^{13}CO(1-0), and C^{18}O(1-0) lines were observed simultaneously with the PMO telescope. The core-average ^{12}CO(1-0), ^{13}CO(1-0), and C^{18}O(1-0) spectra of 30 *Herschel* dense cores are presented in Figure 5. The spectra of ^{12}CO(1-0), ^{13}CO(1-0), and C^{18}O(1-0) are shown in red, green, and blue, respectively. From Gaussian fitting, we obtain peak velocity, full width of half maximum (FWHM), and peak brightness temperature. Some dense cores (17 dense cores) show multiple velocity components; for these we fitted multiple Gaussian components. The fitting parameters of all dense cores are presented in Table 5. For lines with multiple velocity components, the velocity component is determined to be associated with the *Herschel* dense core if its integrated intensity map shows a similar morphology to its *Herschel* map.

The excitation temperature $T_{\rm ex}$ of ^{12}CO is calculated following (Garden et al. 1991)

$$T_{\rm b} = \frac{T_{\rm a}^*}{\eta_b} = \frac{h\nu}{k}\left[\frac{1}{e^{(h\nu/kT_{\rm ex})}-1} - \frac{1}{e^{(h\nu/kT_{\rm bg})}-1}\right] \times (1 - e^{-\tau})f, \quad (4)$$

where $T_{\rm b}$ is the brightness temperature. $T_{\rm bg}$ is the background temperature of 2.73 K. $T_{\rm a}^*$ is the observed antenna temperature, k is the Boltzmann constant, $\eta_{\rm b} = 0.6$ is the main beam efficiency, and ν is the frequency. Assuming that ^{12}CO(1-0) is optically thick ($\tau \gg 1$) and that the filling factor $f = 1$, then $T_{\rm ex}$ can be obtained. The mean, maximum, minimum, and median $T_{\rm ex}$ values of each dense core are presented in Table 6. The mean $T_{\rm ex}$ ranges from 8.5 to 15.1 K, consistent with the dust temperature range.

If we assume that ^{12}CO(1-0) and ^{13}CO(1-0) have the same excitation temperature, the ^{13}CO optical depth can be obtained. These values are also presented in Table 6. Then, the ^{13}CO column density can be calculated as follows (Garden et al. 1991):

$$N = \frac{3k}{8\pi^2 B\mu_{\rm D}^2}\frac{e^{[hBJ(J+1)/kT_{\rm ex}]}}{J+1} \times \frac{T_{\rm ex} + hB/3k}{1 - e^{(-h\nu/kT_{\rm ex})}}\int \tau_v dv, \quad (5)$$

where $B = 55101.012$ MHz is the rotational constant, $\mu_{\rm D} = 0.11$ debyes is the permanent dipole moment for ^{13}CO, and J is the rotational quantum number of the lower state in the observed transition (Chackerian & Tipping 1983). In this paper, we adopt a typical abundance ratio of $[^{12}{\rm CO}]/[^{13}{\rm CO}] = 60$ and $[{\rm H_2}]/[^{12}{\rm CO}] = 10^4$, considering the $[^{12}{\rm CO}]/[^{13}{\rm CO}]$ ratio of ∼50 shown by Hawkins & Jura (1987) for the solar neighborhood and the ratio of ∼70 in the Galaxy shown by Penzias (1980). With these assumptions, the H_2 column densities are calculated and also presented in Table 6. The mean, maximum, minimum, and median values of the column

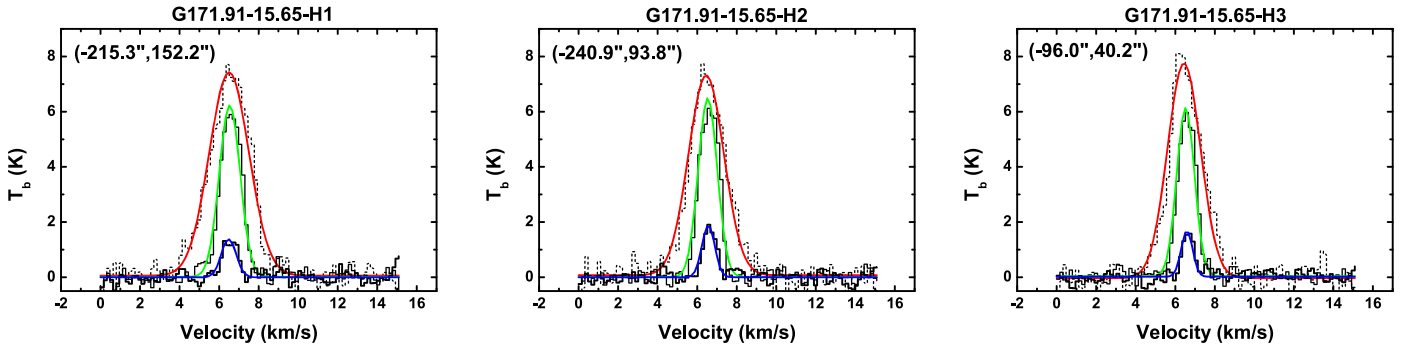

Figure 5. Average spectra of three dense cores for the representative source PGCC G171.91-15.65. The images for other sources are shown in the figure set. For each plot, the three lines of ^{12}CO, ^{13}CO, and C^{18}O are in red, green, and blue, respectively. The offsets of dense cores are presented in the upper left corner in units of arcseconds, and they are measured relative to coordinates of PGCCs released by Planck Collaboration et al. (2016). The core names are provided above each panel. The images for other sources are shown in the figure set.

(The complete figure set (30 images) is available.)

density of each dense core are also given in columns 2 through 5, respectively. The N_{H_2} distributions, derived from PMO data, are presented in panel (b) of Figure 3.

The thermal velocity dispersion (σ_{th}) and non-thermal velocity dispersion (σ_{NT}) are calculated as

$$\sigma_{NT} = \left[\sigma^2_{^{13}CO} - \frac{kT_{ex}}{m_{^{13}CO}}\right]^{1/2}, \quad (6)$$

$$\sigma_{th} = \sqrt{\frac{kT_{ex}}{m_H \mu}}, \quad (7)$$

where $m_{^{13}CO}$ is the mass of the ^{13}CO molecule, m_H is the atomic hydrogen mass, and $\mu = 2.8$ is the mean molecular weight of the gas (Kauffmann et al. 2008). $\sigma_{^{13}CO}$ is the 1D velocity dispersion, obtained from second-moment maps. If the velocity dispersion is isotropic, the 3D velocity dispersions are calculated using

$$\sigma_{3D} = \sqrt{3(\sigma^2_{th} + \sigma^2_{NT})}. \quad (8)$$

The mean, maximum, minimum, and median σ_{NT}, σ_{th}, and σ_{3D} values of each dense core are also presented in Table 6. The mean values of σ_{NT}, derived from ^{13}CO, range from 0.36($\pm$0.09) km s^{-1} to 0.73($\pm$0.07) km s^{-1}. The mean values of σ_{th} range from 0.16($\pm$0.01) to 0.21($\pm$0.01) km s^{-1}.

If ^{13}CO is optically thick, σ_{NT} could be overestimated. Actually, ^{13}CO is optically thick in PGCCs (Wu et al. 2012). The high spectral resolution (0.16 km s^{-1}) in the PMO observations can also resolve the C^{18}O line profiles. Therefore, we also calculated σ_{NT} using C^{18}O data, and the σ_{NT}(C^{18}O) values are presented in Table 8. The σ_{NT}(C^{18}O) values range from 0.19($\pm$0.01) km s^{-1} to 0.71($\pm$0.21) km s^{-1}. The Mach number (σ_{NT} (C^{18}O)/σ_{th}) can be calculated and listed in Table 8, where σ_{th} is the isothermal sound speed. The Mach number of dense cores ranges from 1($\pm$0.08) to 3.8($\pm$1.2), with a mean value of 2.1($\pm$0.8). Thus, we conclude that all the dense cores studied here have supersonic non-thermal motions.

For all of the dense cores, the Mach numbers are always greater than 1, and there is not much difference in Mach number among starless cores, prestellar core candidates, and protostellar cores. The large Mach numbers also indicate that the dense cores may be turbulence-dominated. The non-thermal velocity dispersions, however, could also be caused by bulk motions like infall or rotation.

The integrated intensity maps of C^{18}O(1-0) are shown in panel (c) of Figure 3. The C^{18}O map is very noisy (the average signal-to-noise ratio of the C^{18}O mapping region is 4.1 $\pm$ 1.2). Therefore, it is hard to derive accurate C^{18}O column density maps. Instead, we calculate core-averaged C^{18}O column densities from the core-averaged C^{18}O spectra.

If we assume that C^{18}O emission is optically thin and the excitation temperature is the same as the *Herschel* dust temperature (T_d), the $N_{C^{18}O}$ (column density of C^{18}O) is calculated from Garden et al. (1991) as

$$N_{C^{18}O} = 4.77 \times 10^{13} \frac{(T_{ex} + 0.89)}{e^{(-5.27/T_{ex})}} \int \frac{T_a^*(C^{18}O)}{\eta_b} dv, \quad (9)$$

where T_a^* is antenna temperature, and $\eta_b = 0.6$ is the main beam efficiency of the PMO telescope.

We applied the non-LTE code "Radex" (Van der Tak et al. 2007) to fit C^{18}O parameters. The input parameters for Radex are volume density, kinetic temperature, and line width. We used volume density from *Herschel* observations and assumed that the kinetic temperature equals the dust temperature. The line widths were obtained from Gaussian fits to the PMO C^{18}O(1-0) spectra. The derived column density, excitation temperature, and optical depth from Radex, and the LTE column density derived from PMO data, are summarized in Table 7.

Figure 6 shows the correlation between the LTE C^{18}O column density and the non-LTE C^{18}O column density. The correlation is well fitted by a power-law function, and the fitted function is close to $N_{C^{18}O}$(LTE) = $N_{C^{18}O}$ (non-LTE), which indicates that both the calculations are reasonable.

4. Discussion

4.1. Stabilities Of Dense Cores

The gravitational stability is a critical factor for determining whether a dense core is gravitationally bound or not. Assuming a Gaussian velocity distribution and uniform density distribution, the dense core may be supported solely by random motions. For this configuration, a virial mass can be estimated

Table 5
The Parameters Derived from Spectra of Dense Cores

Name	V_{lsr} (12) (km s^{-1})	FWHM(12) (km s^{-1})	T_b (12) (K)	V_{lsr} (13) (km s^{-1})	FWHM(13) (km s^{-1})	T_b (13) (K)	V_{lsr} (18) (km s^{-1})	FWHM(18) (km s^{-1})	T_b (18) (K)
G166.99-15.34-H1	8.01(±0.01)	0.98(±0.06)	1.8(±0.5)	5.65(±0.04)	2.60(±0.26)	0.3(±0.2)			
	6.38(±0.02)	2.98(±0.04)	4.7(±0.3)	6.64(±0.01)	1.80(±0.04)	1.5(±0.5)	6.93(±0.10)	1.00(±0.38)	0.2(±0.1)
G167.23-15.32-H1	4.42(±0.04)	1.23(±0.12)	3.1(±0.6)	4.23(±0.24)	2.05(±0.53)	0.4(±0.3)			
	6.92(±0.04)	2.97(±0.10)	5.8(±0.4)	6.58(±0.03)	1.54(±0.08)	2.8(±0.3)	6.65(±0.04)	0.53(±0.13)	1.0(±0.3)
G168.00-15.69-H1	4.93(±0.03)	1.22(±0.05)	1.5(±0.8)						
	7.95(±0.01)	1.81(±0.01)	10.1(±0.7)	7.83(±0.01)	0.92(±0.01)	6.4(±0.2)	7.79(±0.01)	0.55(±0.02)	1.8(±0.1)
G168.13-16.39-H1	6.22(±0.01)	1.26(±0.02)	8.3(±0.7)	6.23(±0.01)	0.61(±0.01)	3.9(±0.4)	6.60(±0.01)	0.75(±0.02)	2.8(±0.2)
	7.46(±0.01)	0.92(±0.02)	7.2(±0.7)	7.00(±0.01)	0.90(±0.01)	5.5(±0.3)			
G168.13-16.39-H2	3.60(±0.06)	1.57(±0.13)	2.0(±0.6)						
	6.81(±0.02)	2.09(±0.04)	8.6(±0.5)	6.84(±0.01)	1.24(±0.01)	6.6(±0.3)	6.84(±0.02)	0.88(±0.04)	2.1(±0.2)
G168.72-15.48-H1	7.34(±0.02)	3.04(±0.04)	9.7(±0.5)	7.34(±0.02)	1.28(±0.04)	6.5(±0.5)	7.37(±0.02)	0.57(±0.04)	2.7(±0.4)
G168.72-15.48-H2	7.40(±0.01)	2.74(±0.03)	10.3(±0.4)	7.32(±0.01)	1.27(±0.02)	7.1(±0.4)	7.31(±0.01)	0.68(±0.03)	3.9(±0.3)
G169.43-16.17-H1	5.24(±0.02)	1.80(±0.04)	7.4(±0.8)	5.35(±0.02)	1.42(±0.03)	5.0(±0.8)	5.53(±0.03)	1.30(±0.07)	1.4(±0.2)
	7.76(±0.02)	1.92(±0.05)	6.1(±0.8)	6.93(±0.15)	2.30(±0.18)	1.1(±0.6)			
G169.43-16.17-H2	4.96(±0.02)	1.89(±0.05)	7.8(±0.6)	5.37(±0.01)	1.65(±0.03)	5.6(±0.3)	5.64(±0.03)	0.98(±0.09)	1.6(±0.2)
	7.56(±0.02)	1.63(±0.05)	7.9(±0.7)	7.52(±0.03)	1.29(±0.08)	2.0(±0.3)			
G169.76-16.15-H1	5.21(±0.16)	1.67(±0.16)	7.1(±0.9)	5.52(±0.01)	1.76(±0.03)	5.2(±0.4)	5.69(±0.02)	1.28(±0.06)	1.9(±0.2)
	7.59(±0.16)	1.75(±0.16)	9.3(±0.9)	7.85(±0.03)	1.19(±0.08)	1.8(±0.4)			
G169.76-16.15-H2	5.32(±0.01)	1.39(±0.02)	7.3(±0.6)	5.42(±0.01)	1.05(±0.02)	4.4(±0.8)	5.83(±0.02)	1.15(±0.05)	2.0(±0.2)
	7.56(±0.01)	1.94(±0.03)	9.2(±0.6)	6.71(±0.03)	2.18(±0.05)	3.4(±0.6)			
G169.76-16.15-H3	5.40(±0.01)	1.39(±0.01)	7.6(±0.6)	5.40(±0.01)	0.88(±0.02)	4.5(±0.5)	5.52(±0.01)	0.59(±0.02)	2.2(±0.2)
	7.49(±0.01)	1.61(±0.01)	9.2(±0.6)	6.84(±0.02)	1.88(±0.04)	3.7(±0.3)	6.90(±0.01)	0.72(±0.04)	1.2(±0.1)
G169.76-16.15-H4	5.48(±0.01)	1.38(±0.02)	7.6(±0.5)	5.45(±0.01)	0.67(±0.02)	2.8(±0.5)	5.59(±0.03)	0.58(±0.08)	0.6(±0.2)
	7.58(±0.01)	1.51(±0.02)	8.3(±0.5)	6.83(±0.01)	1.64(±0.03)	3.9(±0.3)	6.88(±0.01)	0.60(±0.03)	1.6(±0.2)
G169.76-16.15-H5	5.57(±0.01)	1.28(±0.03)	7.8(±0.6)	5.59(±0.02)	0.77(±0.03)	3.8(±0.5)	5.71(±0.06)	0.89(±0.13)	0.6(±0.2)
	7.57(±0.02)	1.58(±0.04)	5.9(±0.5)	6.73(±0.02)	1.31(±0.06)	3.9(±0.4)	6.90(±0.02)	0.51(±0.05)	1.3(±0.2)
G170.00-16.14-H1	5.47(±0.02)	1.28(±0.05)	7.6(±0.7)	5.70(±0.12)	1.25(±0.18)	2.8(±0.9)			
	7.36(±0.03)	1.56(±0.07)	5.4(±0.6)	6.78(±0.08)	1.06(±0.11)	3.6(±0.9)	6.59(±0.08)	1.11(±0.13)	0.7(±0.3)
G170.00-16.14-H2	5.30(±0.02)	1.30(±0.04)	7.5(±0.6)	5.31(±0.05)	0.88(±0.11)	1.8(±0.4)			
	7.40(±0.04)	2.12(±0.09)	5.2(±0.5)	6.64(±0.03)	1.56(±0.08)	4.4(±0.4)	6.61(±0.05)	1.11(±0.10)	0.9(±0.2)
G170.13-16.06-H1	5.94(±0.02)	1.48(±0.04)	7.2(±0.5)	6.00(±0.02)	0.96(±0.03)	4.5(±0.4)	5.97(±0.06)	0.62(±0.17)	0.6(±0.3)
	7.38(±0.02)	1.00(±0.04)	4.2(±0.6)	6.96(±0.02)	0.91(±0.03)	4.1(±0.4)	6.85(±0.03)	0.80(±0.07)	1.4(±0.3)
G170.26-16.02-H1	6.23(±0.02)	2.36(±0.04)	6.7(±0.7)	6.36(±0.01)	1.66(±0.02)	5.1(±0.4)	6.64(±0.04)	1.41(±0.09)	1.1(±0.2)
G170.26-16.02-H2	5.99(±0.05)	1.22(±0.08)	6.7(±1.2)	6.51(±0.01)	1.24(±0.01)	5.5(±0.2)	6.56(±0.01)	0.83(±0.04)	1.6(±0.1)
	7.17(±0.06)	1.13(±0.09)	4.9(±1.2)						
G170.83-15.90-H1	6.61(±0.02)	1.46(±0.04)	6.2(±0.4)	6.53(±0.01)	1.06(±0.02)	5.3(±0.3)	6.57(±0.04)	1.17(±0.12)	1.3(±0.3)
G170.83-15.90-H2	6.67(±0.02)	1.73(±0.04)	6.2(±0.5)	6.66(±0.01)	1.18(±0.02)	5.0(±0.2)	6.79(±0.07)	0.95(±0.17)	1.1(±0.3)
G170.99-15.81-H1	5.56(±0.10)	1.06(±0.16)	2.8(±0.4)						
	6.78(±0.06)	1.13(±0.18)	4.3(±0.4)	6.50(±0.01)	1.16(±0.03)	4.8(±0.2)	6.51(±0.02)	0.64(±0.05)	2.2(±0.3)
	8.07(±0.07)	0.71(±0.17)	1.7(±0.8)						
G171.49-14.90-H1	5.95(±0.16)	1.29(±0.16)	7.0(±0.6)	6.52(±0.02)	0.92(±0.04)	5.3(±0.5)	6.55(±0.02)	0.47(±0.04)	2.4(±0.4)
	7.49(±0.16)	1.31(±0.16)	8.4(±0.7)	7.58(±0.03)	0.85(±0.05)	3.2(±0.5)			
G171.80-15.32-H1	6.90(±0.26)	1.77(±0.04)	7.4(±0.5)	6.99(±0.01)	0.96(±0.02)	5.7(±0.3)	6.96(±0.06)	1.22(±0.13)	0.9(±0.2)
G171.80-15.32-H2	9.06(±0.02)	2.17(±0.05)	7.4(±0.5)	7.23(±0.02)	1.29(±0.04)	5.2(±0.3)	7.38(±0.13)	1.67(±0.30)	0.7(±0.3)
G171.80-15.32-H3	7.04(±0.02)	1.96(±0.04)	6.7(±0.4)	7.17(±0.01)	1.01(±0.02)	5.1(±0.3)	7.12(±0.11)	1.44(±0.27)	0.5(±0.3)
G171.91-15.65-H1	6.59(±0.02)	2.36(±0.04)	7.4(±0.4)	6.61(±0.01)	1.25(±0.03)	6.2(±0.3)	6.56(±0.04)	0.90(±0.09)	1.4(±0.3)
G171.91-15.65-H2	6.54(±0.02)	2.12(±0.05)	7.3(±0.4)	6.61(±0.01)	1.14(±0.02)	6.5(±0.3)	6.64(±0.03)	0.78(±0.06)	1.9(±0.3)
G171.91-15.65-H3	6.52(±0.02)	1.97(±0.05)	7.8(±0.4)	6.60(±0.01)	1.06(±0.02)	6.1(±0.3)	6.66(±0.02)	0.69(±0.06)	1.7(±0.3)
G172.06-15.21-H1	6.59(±0.01)	1.72(±0.02)	9.3(±0.2)	6.77(±0.01)	1.01(±0.02)	5.1(±0.2)	6.81(±0.01)	0.57(±0.03)	1.8(±0.2)

Note. All parameters are derived from spectra of dense cores, which averaged over the identified cores' regions. For some dense cores, there are multiple velocity components, but there are some velocity components that do not have ^{13}CO and C^{18}O emission. The spectral plot can be seen in Figure 5.

using (MacLaren et al. 1988)

$$M_{\rm vir} = 2.10 \times 10^2 \left(\frac{R}{\rm pc}\right)\left(\frac{\Delta V}{\rm km\ s^{-1}}\right)^2 M_\odot, \quad (10)$$

where ΔV is the FWHM of C^{18}O spectrum, which is derived from averaged C^{18}O spectra over the *Herschel* dense core, and R is the radius of the *Herschel* dense core. The $M_{\rm vir}$ values of 30 cores range from 3.6(±0.7) $M_\odot$ to 74(±7.6) $M_\odot$ (see Table 8).

We also calculated the virial parameter $\alpha = M_{\rm vir}/M_{\rm core}$. Kauffmann et al. (2013) and Friesen et al. (2016) consider $\alpha = 2$ as a lower limit for gas motions to prevent collapse, unless the dense cores are supported by a significant magnetic field or confined by external pressure. The virial parameter of the dense cores analyzed here ranges from 0.3(±0.1) to 17.5 (±7.3). Fourteen dense cores have virial parameters smaller

Table 6
The Parameters of a Dense Core Derived from CO Gas Emission

Name	N_{H_2} (PMO)				T_{ex}				τ (^{13}CO)	σ_{th}				σ_{NT} (^{13}CO)				σ_{3D} (^{13}CO)			
	mean	max	min	median	mean	max	min	median		mean	max	min	median	mean	max	min	median	mean	max	min	median
	(10^{21} cm^{-2})				(K)					(km s^{-1})				(km s^{-1})				(km s^{-1})			
G166.99-15.34-H1	2.1(±0.2)	2.4	1.7	2.1	8.5(±0.3)	9.0	7.8	8.4	0.34(±0.03)	0.15(±0.003)	0.16	0.14	0.15	0.56(±0.11)	0.83	0.22	0.62	1.02(±0.29)	1.45	0.45	1.11
G167.23-15.32-H1	3.0(±0.4)	3.7	2.2	2.9	10.7(±0.8)	12.5	9.2	10.8	0.48(±0.07)	0.16(±0.007)	0.17	0.15	0.16	0.65(±0.21)	1.26	0.60	0.96	1.17(±0.34)	2.20	1.07	1.69
G168.00-15.69-H1	4.8(±0.3)	5.5	3.9	4.8	15.1(±0.7)	16.8	13.9	14.9	0.78(±0.07)	0.21(±0.005)	0.23	0.21	0.21	0.48(±0.06)	0.62	0.38	0.49	0.91(±0.09)	1.14	0.75	0.92
G168.13-16.39-H1	3.2(±0.3)	4.1	3.0	3.5	12.1(±0.4)	13.4	11.3	12.0	0.58(±0.04)	0.19(±0.004)	0.20	0.19	0.19	0.37(±0.04)	0.44	0.27	0.38	0.73(±0.06)	0.83	0.58	0.73
G168.13-16.39-H2	3.5(±0.3)	4.1	3.1	3.5	12.5(±0.7)	14.1	11.4	12.3	1.30(±0.20)	0.19(±0.005)	0.21	0.19	0.19	0.36(±0.06)	0.48	0.26	0.37	0.70(±0.09)	0.91	0.55	0.72
G168.72-15.48-H1	6.8(±0.5)	8.1	5.6	6.9	14.4(±0.4)	16.6	12.3	14.3	1.03(±0.07)	0.21(±0.003)	0.73	0.19	0.21	0.73(±0.07)	0.89	0.37	0.75	1.32(±0.12)	1.59	0.73	1.35
G168.72-15.48-H2	6.8(±0.6)	7.8	5.9	6.9	14.9(±0.7)	16.6	13.7	14.9	0.84(±0.07)	0.21(±0.005)	0.22	0.20	0.21	0.67(±0.09)	0.82	0.43	0.67	1.21(±0.15)	1.47	0.84	1.21
G169.43-16.17-H1	6.1(±0.4)	7.0	5.3	6.0	11.0(±0.4)	12.1	10.1	11.0	1.07(±0.10)	0.18(±0.003)	0.19	0.18	0.18	0.58(±0.05)	0.66	0.46	0.59	1.05(±0.08)	1.19	0.85	1.07
G169.43-16.17-H2	1.8(±0.3)	2.1	1.1	1.8	11.9(±0.8)	13.7	10.6	11.8	1.07(±0.17)	0.19(±0.006)	0.19	0.18	0.19	0.40(±0.16)	0.70	0.46	0.65	0.77(±0.24)	1.27	1.00	1.18
G169.76-16.15-H1	5.3(±0.4)	5.9	4.5	5.2	11.2(±0.6)	12.7	10.1	11.0	1.09(±0.15)	0.18(±0.005)	0.20	0.18	0.18	0.53(±0.04)	0.60	0.47	0.53	0.98(±0.07)	1.09	0.87	0.97
G169.76-16.15-H2	4.8(±0.2)	5.2	4.4	4.9	11.0(±0.6)	12.4	10.1	10.8	0.85(±0.10)	0.18(±0.005)	0.19	0.18	0.18	0.47(±0.04)	0.56	0.41	0.47	0.88(±0.06)	1.01	0.78	0.86
G169.76-16.15-H3	3.5(±0.3)	4.1	2.9	3.5	12.9(±0.9)	14.4	10.6	13.0	0.48(±0.06)	0.20(±0.007)	0.19	0.18	0.18	0.51(±0.07)	0.54	0.38	0.47	0.95(±0.11)	0.99	0.74	0.87
G169.76-16.15-H4	3.2(±0.2)	3.8	2.8	3.2	11.6(±0.7)	12.5	10.2	11.8	0.66(±0.08)	0.19(±0.006)	0.20	0.18	0.19	0.49(±0.11)	0.59	0.27	0.48	0.91(±0.18)	1.06	0.57	0.89
G169.76-16.15-H5	2.5(±0.3)	3.0	2.0	2.6	10.2(±0.7)	11.2	9.4	10.3	0.81(±0.13)	0.18(±0.005)	0.20	0.18	0.19	0.45(±0.14)	0.57	0.37	0.45	0.84(±0.23)	1.05	0.72	0.85
G170.00-16.14-H1	3.7(±0.3)	4.0	3.2	3.8	11.4(±0.6)	12.4	10.4	11.7	0.59(±0.06)	0.19(±0.005)	0.20	0.18	0.19	0.52(±0.18)	0.69	0.16	0.64	0.97(±0.28)	1.24	0.42	1.16
G170.00-16.14-H2	3.8(±0.7)	4.7	2.4	3.7	11.6(±0.8)	13.8	10.7	11.4	0.76(±0.11)	0.19(±0.007)	0.21	0.18	0.19	0.59(±0.10)	0.67	0.31	0.62	1.07(±0.16)	1.20	0.62	1.12
G170.13-16.06-H1	5.0(±0.4)	5.9	3.9	5.0	11.4(±0.7)	12.8	10.1	11.5	0.72(±0.09)	0.19(±0.006)	0.20	0.18	0.19	0.55(±0.04)	0.63	0.44	0.56	1.01(±0.07)	1.13	0.82	1.02
G170.26-16.02-H1	3.9(±0.3)	4.2	3.6	3.8	11.4(±0.6)	12.3	10.6	11.4	1.01(±0.12)	0.18(±0.005)	0.22	0.16	0.18	0.43(±0.02)	0.77	0.30	0.43	0.82(±0.08)	1.38	0.60	0.82
G170.26-16.02-H2	4.2(±0.1)	4.5	3.9	4.2	10.6(±0.5)	11.4	9.7	10.7	1.42(±0.21)	0.18(±0.004)	0.19	0.17	0.18	0.46(±0.05)	0.54	0.32	0.48	0.86(±0.09)	0.98	0.63	0.88
G170.83-15.90-H1	1.7(±0.4)	2.4	9.3	1.7	9.6(±0.8)	11.4	8.5	9.5	1.81(±0.65)	0.17(±0.007)	0.19	0.16	0.17	0.39(±0.14)	0.58	0.07	0.41	0.74(±0.22)	1.05	0.31	0.76
G170.83-15.90-H2	1.3(±0.4)	2.3	3.2	1.3	10.2(±0.9)	12.4	8.1	10.2	1.28(±0.32)	0.18(±0.008)	0.19	0.16	0.18	0.37(±0.11)	0.69	0.11	0.39	0.72(±0.18)	1.24	0.34	0.73
G170.99-15.81-H1	3.8(±0.9)	5.8	2.0	3.7	8.9(±1.0)	11.6	7.1	8.8	1.89(±1.01)	0.16(±0.010)	0.19	0.15	0.16	0.58(±0.18)	0.94	0.14	0.61	1.05(±0.30)	1.65	0.38	1.09
G171.49-14.90-H1	4.5(±0.5)	5.1	3.8	4.5	12.4(±0.8)	14.0	11.6	12.2	0.88(±0.12)	0.19(±0.006)	0.20	0.18	0.18	0.51(±0.08)	0.54	0.14	0.38	0.95(±0.13)	0.99	0.39	0.73
G171.80-15.32-H1	3.9(±0.5)	4.5	3.3	3.8	12.1(±0.7)	13.6	11.0	12.0	1.05(±0.14)	0.19(±0.005)	0.20	0.18	0.19	0.43(±0.13)	0.66	0.20	0.44	0.81(±0.20)	1.18	0.48	0.83
G171.80-15.32-H2	4.5(±0.3)	5.0	4.2	4.5	11.4(±0.6)	12.9	10.6	11.5	1.02(±0.13)	0.19(±0.005)	0.20	0.18	0.19	0.65(±0.06)	0.75	0.46	0.66	1.16(±0.11)	1.32	0.86	1.19
G171.80-15.32-H3	3.7(±0.3)	4.2	3.1	3.6	10.8(±0.4)	11.6	10.3	10.7	1.14(±0.10)	0.18(±0.003)	0.19	0.18	0.18	0.66(±0.07)	0.76	0.53	0.66	1.19(±0.11)	1.36	0.97	1.18
G171.91-15.65-H1	4.8(±0.3)	5.3	4.3	4.6	11.4(±0.5)	12.3	10.8	11.4	1.49(±0.19)	0.19(±0.004)	0.19	0.18	0.19	0.42(±0.09)	0.52	0.27	0.43	0.80(±0.13)	0.96	0.57	0.81

Table 6
(Continued)

Name	N_{H_2} (PMO)				T_{ex}				τ (^{13}CO)	σ_{th}				σ_{NT} (^{13}CO)				σ_{3D} (^{13}CO)			
	mean	max	min	median	mean	max	min	median		mean	max	min	median	mean	max	min	median	mean	max	min	median
	(10^{21} cm^{-2})				(K)					(km s^{-1})				(km s^{-1})				(km s^{-1})			
G171.91-15.65-H2	4.6(±0.5)	5.3	3.6	4.7	11.3(±0.4)	12.1	10.9	11.3	1.64(±0.19)	0.19(±0.003)	0.19	0.18	0.19	0.43(±0.08)	0.53	0.27	0.43	0.80(±0.14)	0.97	0.13	0.80
G171.91-15.65-H3	4.4(±0.2)	4.5	3.8	4.2	12.2(±0.5)	13.0	11.0	12.1	1.16(±0.12)	0.19(±0.004)	0.20	0.18	0.19	0.36(±0.09)	0.48	0.23	0.40	0.71(±0.14)	0.89	0.52	0.77
G172.06-15.21-H1	3.7(±0.3)	4.3	3.2	3.7	13.3(±0.4)	13.9	12.4	13.2	0.71(±0.05)	0.20(±0.003)	0.21	0.20	0.20	0.41(±0.06)	0.52	0.31	0.41	0.79(±0.09)	0.97	0.64	0.79

Note. All of these parameters are derived from the PMO observational data. Excitation temperature is calculated by ^{12}CO data, and N_{H_2}(PMO), σ_{NT}, and σ_{3D} are derived from ^{13}CO images.

Table 7
The Parameters of $C^{18}O$ Molecules

Name	$N_{C^{18}O}$ (LTE) (10^{14} cm^{-2})	$C^{18}O$ Abundance(LTE) (10^{-7})	f_D	τ ($C^{18}O$)	T_{ex} (non-LTE)($C^{18}O$) (K)	$N_{C^{18}O}$ (non-LTE) (10^{15} cm^{-2})
G166.99-15.34-H1	1.59(±0.22)	0.44(±0.18)	6.59(±1.75)	0.02	13.99	0.15
G167.23-15.32-H1	4.92(±0.40)	0.66(±0.26)	4.36(±1.16)	0.10	13.02	0.18
G168.00-15.69-H1	9.92(±0.11)	1.69(±0.42)	1.69(±0.45)	0.2.	12.31	1.02
G168.13-16.39-H1	19.63(±0.17)	1.28(±0.34)	2.24(±0.59)	0.38	12.06	2.54
G168.13-16.39-H2	17.16(±0.15)	1.29(±0.15)	2.22(±0.59)	0.28	11.80	2.02
G168.72-15.48-H1	17.62(±0.19)	1.26(±0.21)	2.28(±0.61)	0.37	12.08	2.24
G168.72-15.48-H2	22.32(±1.55)	0.91(±0.29)	3.17(±0.84)	0.50	13.31	3.11
G169.43-16.17-H1	16.88(±0.24)	1.61(±0.38)	1.78(±0.47)	0.17	12.25	1.83
G169.43-16.17-H2	14.58(±0.36)	1.48(±0.31)	1.95(±0.52)	0.20	12.12	1.66
G169.76-16.15-H1	22.89(±0.23)	2.35(±0.31)	1.22(±0.32)	0.24	12.19	2.69
G169.76-16.15-H2	22.05(±0.10)	2.31(±0.23)	1.24(±0.33)	0.24	12.53	2.54
G169.76-16.15-H3	8.42(±0.15)	0.80(±0.21)	3.58(±0.95)	0.14	12.43	0.96
G169.76-16.15-H4	9.23(±0.15)	0.83(±0.19)	3.46(±0.92)	0.21	12.05	1.10
G169.76-16.15-H5	6.25(±0.16)	0.55(±0.18)	5.20(±1.38)	0.16	12.20	0.74
G170.00-16.14-H1	7.56(±0.29)	0.61(±0.17)	4.70(±1.25)	0.10	11.25	0.89
G170.00-16.14-H2	9.24(±0.66)	0.74(±0.30)	3.89(±1.03)	0.10	12.38	1.08
G170.13-16.06-H1	10.43(±0.31)	0.90(±0.23)	3.18(±0.84)	0.18	11.79	1.18
G170.26-16.02-H1	14.64(±0.34)	1.21(±0.28)	1.95(±0.52)	0.14	11.57	1.74
G170.26-16.02-H2	1.22(±0.22)	0.99(±0.32)	2.91(±0.77)	0.22	11.23	1.52
G170.83-15.90-H1	15.08(±0.41)	2.87(±0.76)	1.00(±0.27)	0.16	12.55	1.59
G170.83-15.90-H2	10.04(±0.49)	1.86(±0.36)	1.54(±0.41)	0.13	12.66	1.09
G170.99-15.81-H1	13.12(±0.28)	1.61(±0.40)	1.79(±0.47)	0.30	11.72	1.48
G171.49-14.90-H1	10.21(±0.34)	0.48(±0.17)	5.97(±1.58)	0.36	11.35	1.44
G171.80-15.32-H1	9.82(±0.41)	0.66(±0.25)	4.37(±1.16)	0.12	11.24	1.17
G171.80-15.32-H2	10.82(±1.44)	1.21(±0.37)	2.36(±0.63)	0.08	12.76	1.23
G171.80-15.32-H3	11.82(±0.29)	0.88(±0.11)	3.25(±0.86)	0.06	11.37	0.72
G171.91-15.65-H1	12.82(±0.51)	1.64(±0.60)	1.75(±0.46)	0.14	14.10	1.48
G171.91-15.65-H2	13.82(±0.66)	1.42(±0.68)	2.03(±0.54)	0.21	13.47	1.80
G171.91-15.65-H3	14.82(±0.13)	1.80(±0.17)	1.60(±0.42)	0.20	12.69	1.26
G172.06-15.21-H1	15.82(±0.17)	1.83(±0.35)	1.57(±0.42)	0.22	12.39	1.13

Note. The LTE parameters are derived from $C^{18}O$ spectra. The non-LTE parameters and $\tau(C^{18}O)$ are derived from the "Radex" software. The depletion factor (f_D) is calculated by $N_{C^{18}O}$(LTE).

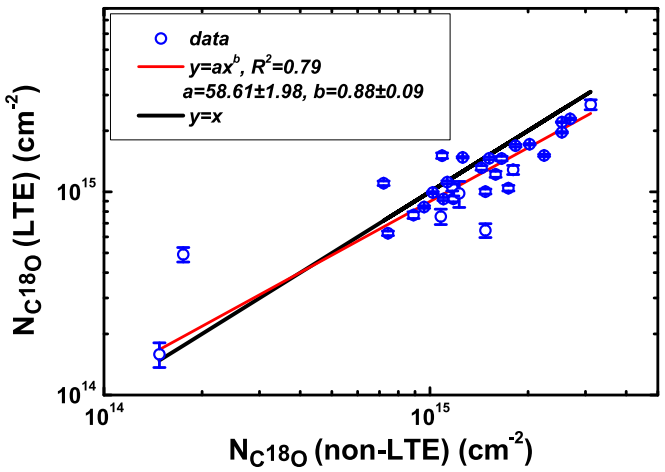

Figure 6. Relationship of the LTE $C^{18}O$ column density and the non-LTE $C^{18}O$ column density for all of the 30 dense cores in PGCCs. The red solid line is a power-law fit. Each blue dot represents a single dense core. The black solid line is $N_{C^{18}O}$(LTE) = $N_{C^{18}O}$ (non-LTE). The models are presented in the upper left corner of the figure. A strong correlation can be seen very close to $N_{C^{18}O}$ (LTE) = $N_{C^{18}O}$ (non-LTE), which indicates that the LTE $C^{18}O$ column density estimates are reasonable.

than 2 and hence are gravitationally bound and may collapse. In Figure 7, we plot M_{core} against M_{vir} and the black dashed line indicates $M_{vir} = 2M_{core}$. We find that some protostellar cores and prestellar core candidates have virial parameters larger than 2. This apparent discrepancy might be due to the following factors:

1. Turbulence contributions. Turbulence is only dissipated in the densest regions of clouds, while the PMO observations cannot resolve such small-scale dense regions. The size of the $C^{18}O$ core can be larger than the *Herschel* continuum core such that the $C^{18}O$ line width may include significant contributions from its turbulent surroundings. For example, Pattle et al. (2015) found that non-thermal line widths decrease substantially between the gas traced by $C^{18}O$ and that traced by N_2H^+ in the dense cores of the Ophiuchus molecular cloud, indicating the dissipation of turbulence at higher densities.
2. $C^{18}O$ depletion. The depletion of $C^{18}O$ at the inner core region makes the $C^{18}O$(1-0) line a poor tracer at those locations. Thus, the $C^{18}O$ line width is determined more by the gaseous outer, more turbulent regions. The presence of a central region affected by strong CO depletion could be the most important factor of uncertainty in the virial parameter (Giannetti et al. 2014).

Both of these factors can lead to an overestimation of the virial parameter. $C^{18}O$ lines, however, have often been used for virial analysis. For comparison, we plot the data from Onishi et al. (1996), Tachihara et al. (2000), and Zhang et al. (2015) in gray stars, orange circles, and black triangles,

Table 8
The Parameters of the Dense Cores

Name	V_{lsr} ($C^{18}O$) (km s^{-1})	M_{vir} ($M_{\odot}$)	α	Jeans Length (pc)	σ_{NT} ($C^{18}O$) (km s^{-1})	Mach Number[a]
G166.99-15.34-H1	6.93(±0.10)	23.49(±17.76)	6.50(±5.20)	0.375(±0.011)	0.43(±0.32)	2.66(±2.05)
G167.23-15.32-H1	6.65(±0.04)	6.48(±3.06)	0.97(±0.49)	0.249(±0.007)	0.22(±0.03)	1.22(±0.20)
G168.00-15.69-H1	7.79(±0.01)	16.82(±1.21)	0.58(±0.04)	0.440(±0.010)	0.23(±0.01)	1.04(±0.05)
G168.13-16.39-H1	6.60(±0.01)	20.20(±1.02)	0.58(±0.03)	0.207(±0.006)	0.32(±0.01)	1.65(±0.07)
G168.13-16.39-H2	6.84(±0.02)	35.58(±3.31)	0.98(±0.09)	0.244(±0.004)	0.37(±0.02)	1.92(±0.14)
G168.72-15.48-H1	7.37(±0.02)	16.66(±1.22)	0.63(±0.05)	0.214(±0.005)	0.28(±0.01)	1.37(±0.05)
G168.72-15.48-H2	7.31(±0.01)	9.49(±1.27)	0.25(±0.03)	0.164(±0.013)	0.24(±0.01)	1.11(±0.06)
G169.43-16.17-H1	5.53(±0.03)	74.28(±7.64)	2.45(±0.26)	0.275(±0.006)	0.56(±0.15)	3.04(±0.89)
G169.43-16.17-H2	5.64(±0.03)	28.21(±5.30)	2.28(±0.45)	0.231(±0.005)	0.42(±0.05)	2.19(±0.31)
G169.76-16.15-H1	5.69(±0.02)	37.45(±3.46)	5.78(±0.62)	0.205(±0.004)	0.55(±0.19)	2.96(±1.10)
G169.76-16.15-H2	5.83(±0.02)	32.81(±2.56)	4.64(±0.42)	0.222(±0.002)	0.49(±0.04)	2.69(±0.30)
G169.76-16.15-H3	6.90(±0.01)	11.85(±1.15)	1.26(±0.14)	0.202(±0.005)	0.30(±0.01)	1.53(±0.11)
G169.76-16.15-H4	6.88(±0.01)	7.97(±0.78)	0.91(±0.10)	0.189(±0.005)	0.25(±0.01)	1.33(±0.09)
G169.76-16.15-H5	6.90(±0.02)	3.86(±0.73)	0.87(±0.20)	0.157(±0.004)	0.21(±0.01)	1.19(±0.10)
G170.00-16.14-H1	6.59(±0.08)	16.00(±3.62)	4.97(±1.37)	0.128(±0.004)	0.47(±0.09)	2.54(±0.56)
G170.00-16.14-H2	6.61(±0.05)	16.68(±3.01)	3.66(±0.81)	0.143(±0.009)	0.47(±0.07)	2.51(±0.46)
G170.13-16.06-H1	6.85(±0.03)	25.16(±4.34)	0.94(±0.17)	0.240(±0.007)	0.34(±0.03)	1.82(±0.19)
G170.26-16.02-H1	6.64(±0.04)	20.28(±2.53)	15.08(±3.43)	0.146(±0.004)	0.60(±0.10)	3.28(±0.63)
G170.26-16.02-H2	6.56(±0.01)	12.67(±1.07)	1.63(±0.17)	0.153(±0.006)	0.35(±0.02)	1.97(±0.13)
G170.83-15.90-H1	6.57(±0.04)	35.56(±7.05)	7.09(±1.66)	0.305(±0.007)	0.50(±0.23)	2.92(±1.48)
G170.83-15.90-H2	6.79(±0.07)	18.27(±6.41)	4.53(±1.68)	0.267(±0.006)	0.40(±0.09)	2.30(±0.61)
G170.99-15.81-H1	6.51(±0.02)	26.87(±3.84)	0.45(±0.07)	0.377(±0.009)	0.27(±0.02)	1.66(±0.20)
G171.49-14.90-H1	6.55(±0.02)	3.60(±0.65)	0.36(±0.07)	0.111(±0.004)	0.19(±0.01)	1.00(±0.08)
G171.80-15.32-H1	6.96(±0.06)	25.72(±5.42)	3.27(±0.77)	0.134(±0.005)	0.52(±0.12)	2.72(±0.72)
G171.80-15.32-H2	7.38(±0.13)	35.66(±12.67)	17.46(±7.27)	0.167(±0.010)	0.71(±0.21)	3.83(±1.20)
G171.80-15.32-H3	7.12(±0.11)	50.51(±19.20)	4.47(±1.75)	0.169(±0.004)	0.62(±0.25)	3.40(±1.42)
G171.91-15.65-H1	6.56(±0.04)	7.50(±1.45)	6.17(±2.15)	0.169(±0.005)	0.38(±0.04)	2.06(±0.24)
G171.91-15.65-H2	6.64(±0.03)	6.40(±0.96)	2.56(±0.58)	0.157(±0.007)	0.33(±0.02)	1.76(±0.13)
G171.91-15.65-H3	6.66(±0.02)	9.61(±1.53)	2.27(±0.41)	0.218(±0.002)	0.29(±0.02)	1.50(±0.11)
G172.06-15.21-H1	6.81(±0.01)	7.30(±0.79)	0.94(±0.12)	0.219(±0.006)	0.24(±0.01)	1.18(±0.05)

Note. α is calculated by M_{vir}/M_{core}, and the other parameters are derived from $C^{18}O$ data.
[a] The Mach numbers are derived from $\sigma_{NT}(C^{18}O)/\sigma_{th}$.

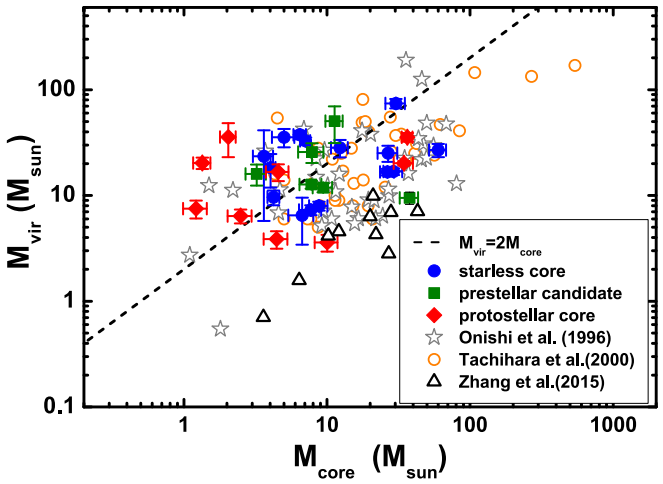

Figure 7. Relationship between the M_{core} and M_{vir} of dense cores. The red diamonds, green squares, and blue dots represent the protostellar cores, prestellar core candidates, and starless cores, respectively. The gray stars, orange circles, and black triangles are data from Onishi et al. (1996), Tachihara et al. (2000), and Zhang et al. (2015), respectively. The black dashed line indicates $M_{vir} = 2M_{core}$. The virial parameter $\alpha = 2$ can be regarded as a lower limit for gas motions to prevent collapse.

respectively, in Figures 7 and 8. The virial masses in those works were also calculated with $C^{18}O$ lines. In contrast to dense cores in other works, the cores in L1495 have similar but relatively larger virial parameters. We found that dense cores in far-away infrared dark clouds (Zhang et al. 2015; Ohashi et al. 2016; Sanhueza et al. 2017) have much smaller virial parameters than Taurus cores, suggesting that infrared dark clouds have much denser environments for star formation. A survey by Fehér et al. (2017) found that 5 out of 21 PGCCs are gravitationally bound, based on *Herschel* and CO data.

As we mentioned before, the turbulence is dissipated in denser regions, $C^{18}O$ is affected by turbulence from outer regions, and turbulence is also significantly affected by $C^{18}O$ depletion. Observations of this region in nitrogen-bearing tracers with comparable resolution were presented by Seo et al. (2015). A total of 12 dense cores in our samples correspond to theirs. The mean value of non-thermal velocity dispersion derived from their NH_3 and our $C^{18}O$ are 0.20(±0.02) km s^{-1} and 0.39 ± 0.15 km s^{-1}, respectively. This suggests that turbulence is considerably dissipated in more centered regions. The $C^{18}O$ in these regions was depleted, and non-thermal velocity dispersion derived from $C^{18}O$ mainly came from from diffused gas. Together with the above comparison, $C^{18}O$ lines may be not good indicators of the virial parameter, especially for prestellar and protostellar cores. To clarify the situation, high-resolution observations of dense gas tracers (e.g., N_2H^+) are needed.

Kauffmann et al. (2013) compiled a catalog containing 1325 virial estimates for entire molecular clouds (≫1 pc scale),

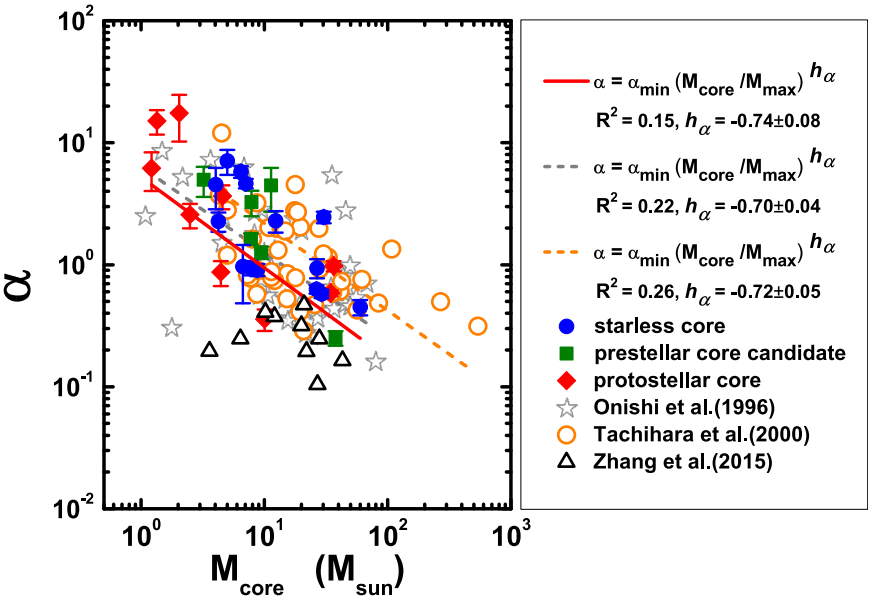

Figure 8. Relationship between $M_{\rm core}$ and α. The red diamonds, green squares, and blue dots represent the protostellar cores, prestellar core candidates, and starless cores, respectively. The gray stars, orange circles, and black triangles are data from Onishi et al. (1996), Tachihara et al. (2000), and Zhang et al. (2015) respectively. The red solid, gray, and orange dashed lines indicate power-law fitting of $\alpha = \alpha_{\rm min} \cdot (M_{\rm core}/M_{\rm max})^{h_\alpha}$ for L1495 samples, gray stars, and orange circles, respectively.

clumps ($\sim$1 pc), and cores ($\ll$1 pc). They suggested an anti-correlation exists between mass and virial parameter:

$$\alpha = \alpha_0 \cdot (M/10^3\,M_\odot)^{h_\alpha}, \tag{11}$$

with a similar slope h_α, and α_0 is a range of intercepts. To highlight the trend, the equation above can be rewritten as

$$\alpha = \alpha_{\rm min} \cdot (M/M_{\rm max})^{h_\alpha}, \tag{12}$$

where $\alpha_0 = \alpha_{\rm min} \cdot (M_{\rm max}/10^3\,M_\odot)^{-h_\alpha}$. We fit this power-law function to our 30 samples and data from Onishi et al. (1996) and Tachihara et al. (2000); the fitting results are presented in Figure 8. Data from Zhang et al. (2015) were excluded from the fitting due to there being too few data points to fit. The virial parameters from our work, Onishi et al. (1996), and Tachihara et al. (2000) follow the above power-law behavior, with slopes h_α of $-0.74(\pm0.08)$, $-0.70(\pm0.04)$, and $-0.72(\pm0.05)$, respectively. This is consistent with the range $0 < -h_\alpha < 1$ reported in Kauffmann et al. (2013). Similar relationships between virial parameters and core masses were also reported by Loren (1989) and Bertoldi & Mckee (1992). According to Figure 8, we found that these cores also show similar power-law behaviors, indicating that these samples have similar physical properties. In Figures 7 and 8, the black triangles (Zhang et al. 2015) have the lowest virial parameters, and they indicate higher star-forming activity, such as outflows. This may indicate that our dense cores are at an evolutionary stage that is much earlier than those of the cores reported by Zhang et al. (2015).

We also calculated the thermal Jeans length (Jeans 1928) of dense cores; see Table 8. We found that the radii of 30 dense cores are smaller than the thermal Jeans length. Considering that all dense core have supersonic non-thermal motions, this may indicate that the non-thermal motions are capable of creating an effectively hydrostatic pressure that opposes core-collapse (Mac Low & Klessen 2004).

4.2. Column Density Profile

In this section, we study the density profiles of the dense cores. We averaged the *Herschel* column density data in concentric elliptical bins to get a column density profile, and then fitted the Spherical Geometry Model of Dapp & Basu (2009). The underlying model resembles the Bonnor–Ebert model in that it features a flat central region, leading into a power-law decline $\propto r^{-2}$ in density, and a well-defined outer radius. The model can overcome the Bonnor–Ebert profile in several ways. However, this model does not assume that the cloud is in equilibrium, and can instead make qualitative statements about its dynamical state (expansion, equilibrium, collapse) using the size of the flat region as a proxy (Dapp & Basu 2009). Therefore, it is more suitable to study the properties of dense cores in different dynamical states.

The basic model is

$$n(r) = \begin{cases} n_{\rm c} a^2/(r^2 + a^2) & r \leqslant R_{\rm t} \\ 0 & r > R_{\rm t}, \end{cases} \tag{13}$$

which is characterized by a central volume density $n_{\rm c}$ and a truncated radius $R_{\rm t}$ (To avoid confusion with the core radius from Gaussian fits, we use $R_{\rm t}$ to represent the truncated radius of cores derived from density profiles). The parameter a represents the size of the inner flat region of a dense core. The column density N_x can be derived by integrating the volume density along the line of sight through the sphere. Introducing the parameter $c \equiv R_{\rm t}/a$, $N_{\rm c} = 2an_{\rm c}\arctan(c)$. Hence, the model can be rewritten as

$$N_x = \frac{N_{\rm c}}{\sqrt{1 + (x/a)^2}} \times \left[\arctan\left(\sqrt{\frac{c^2 - (x/a)^2}{1 + (x/a)^2}}\right) \Big/ \arctan(c)\right], \tag{14}$$

Table 9
The Parameters Derived from Column Density Profiles

Name	N_c (10^{22} cm^{-2})	R_t [a] (pc)	a (pc)	n_c [b] (10^4 cm^{-3})	a_d [c] (pc)	R_d [d] (pc)
G166.99-15.34-H1	0.66(±0.01)	0.12(±0.04)	0.028(±0.002)	2.88(±0.38)	0.025(±0.002)	0.12(±0.04)
G167.23-15.32-H1	1.19(±0.01)	0.10(±0.01)	0.045(±0.001)	3.77(±0.12)	0.043(±0.001)	0.10(±0.01)
G168.00-15.69-H1	0.91(±0.01)	0.28(±0.04)	0.089(±0.005)	1.31(±0.11)	0.089(±0.005)	0.28(±0.04)
G168.13-16.39-H1	2.68(±0.01)	0.38(±0.04)	0.038(±0.002)	7.79(±0.45)	0.036(±0.002)	0.40(±0.04)
G168.13-16.39-H2	1.62(±0.01)	0.25(±0.03)	0.043(±0.006)	4.35(±0.64)	0.042(±0.006)	0.25(±0.03)
G168.72-15.48-H1	2.10(±0.01)	0.93(±0.67)	0.048(±0.017)	4.65(±1.75)	0.047(±0.017)	0.92(±0.67)
G168.72-15.48-H2	4.51(±0.02)	0.37(±0.25)	0.028(±0.001)	17.74(±1.30)	0.025(±0.001)	0.37(±0.25)
G169.43-16.17-H1	1.51(±0.01)	0.19(±0.04)	0.083(±0.007)	2.56(±0.35)	0.082(±0.007)	0.19(±0.04)
G169.43-16.17-H2	1.41(±0.01)	0.09(±0.04)	0.039(±0.017)	5.02(±2.23)	0.037(±0.018)	0.09(±0.04)
G169.76-16.15-H1	1.20(±0.01)	0.88(±0.44)	0.048(±0.006)	2.65(±0.30)	0.047(±0.005)	0.88(±0.44)
G169.76-16.15-H2	1.13(±0.01)	0.99(±0.36)	0.053(±0.005)	2.26(±0.24)	0.052(±0.005)	0.99(±0.36)
G169.76-16.15-H3	1.80(±0.01)	0.29(±0.11)	0.029(±0.001)	6.95(±0.43)	0.026(±0.001)	0.29(±0.11)
G169.76-16.15-H4	1.73(±0.01)	0.29(±0.23)	0.029(±0.002)	6.50(±0.72)	0.027(±0.002)	0.29(±0.23)
G169.76-16.15-H5	2.18(±0.03)	0.10(±0.05)	0.018(±0.001)	14.06(±1.93)	0.014(±0.002)	0.10(±0.05)
G170.00-16.14-H1	1.86(±0.02)	0.09(±0.02)	0.026(±0.002)	9.11(±1.03)	0.023(±0.002)	0.09(±0.02)
G170.00-16.14-H2	2.36(±0.03)	0.06(±0.01)	0.022(±0.002)	14.19(±1.35)	0.019(±0.002)	0.06(±0.01)
G170.13-16.06-H1	1.61(±0.04)	0.13(±0.01)	0.085(±0.012)	3.11(±0.44)	0.084(±0.012)	0.13(±0.01)
G170.26-16.02-H2	2.30(±0.01)	0.12(±0.01)	0.027(±0.001)	10.41(±0.33)	0.024(±0.001)	0.12(±0.01)
G170.83-15.90-H1	0.72(±0.01)	0.13(±0.03)	0.049(±0.004)	1.95(±0.26)	0.048(±0.004)	0.13(±0.03)
G170.83-15.90-H2	0.96(±0.01)	0.18(±0.09)	0.032(±0.002)	3.47(±0.38)	0.030(±0.002)	0.18(±0.09)
G170.99-15.81-H1	1.36(±0.01)	0.26(±0.05)	0.050(±0.002)	3.16(±0.22)	0.049(±0.002)	0.26(±0.05)
G171.49-14.90-H1	3.79(±0.03)	0.11(±0.01)	0.025(±0.001)	18.11(±0.56)	0.022(±0.001)	0.11(±0.01)
G171.80-15.32-H1	2.61(±0.04)	0.10(±0.01)	0.031(±0.002)	10.65(±0.73)	0.029(±0.002)	0.10(±0.01)
G171.80-15.32-H2	1.37(±0.01)	0.17(±0.08)	0.027(±0.002)	5.96(±0.72)	0.024(±0.002)	0.16(±0.08)
G171.80-15.32-H3	1.91(±0.01)	0.23(±0.03)	0.030(±0.001)	7.13(±0.28)	0.028(±0.001)	0.23(±0.03)
G171.91-15.65-H2[e]	2.43(±0.06)	0.11(±0.08)	0.010(±0.001)	27.29(±4.08)	...	0.11(±0.08)
G171.91-15.65-H3	1.00(±0.01)	0.90(±0.27)	0.043(±0.002)	2.46(±0.13)	0.041(±0.002)	0.90(±0.27)
G172.06-15.21-H1	1.51(±0.03)	0.27(±0.09)	0.025(±0.002)	6.76(±0.67)	0.021(±0.002)	0.27(±0.08)

Notes. All of these parameters come from a fit to a column density profile. The column density profiles are derived from a *Herschel* column density map. Due to the small size of G170.26-16.02-H1 and G171.91-16.15-H1, we cannot obtain their average column density distributions. Thus, we only present the parameters of 28 dense cores in this table.

[a] The truncated radii are derived from fitting to a column density profile.

[b] The central volume density as calculated by $n_c = N_c/2a \arctan(c)$, $c \equiv R/a$.

[c] a_d represents the flat region that was removed by the beam effect using $a_d = (a^2 - \text{beam}^2)^{1/2}$.

[d] R_d represents the flat region that was removed by the beam effect using $R_d = (R^2 - \text{beam}^2)^{1/2}$.

[e] The flat region a of G171.91-15.65-core2 is smaller than the beam size (0.012 pc), so we cannot calculate the a_d.

where N_c, R_t, and a are free parameters. Due to their small sizes, we cannot obtain average column density distributions for G170.26-16.02-H1 and G171.91-16.15-H1. Therefore, we only fit *Herschel* column density profiles to the other 28 cores in this section. N_c, R_t, a, and n_c are shown in Table 9, and the statistics of these parameters are summarized in Table 10.

The beam size is a critical factor that can affect the column density profile. For example, the resolution of the column density maps from *Herschel* data sets a lower limit for the size of the flat region a and the core truncated radius R_t. To remove the beam effect, we use a quadratic rule, $a_d = (a^2 - \theta^2_{\text{beam}})^{1/2}$, to compute the deconvolved size of the flat region a_d. A similar method was also used to calculate the deconvolved core radius R_d (a_d and R_d are listed in Table 9). Since the measured flat region of G171.91-15.65-H2 is smaller than the beam size, we cannot compute its a_d, and that core was also excluded from further analyses. Therefore, we present the column density profiles of G171.91-15.65-H3 in Figure 9. The profiles for other dense cores are shown in the figure set.

The upper, middle, and bottom panels of Figure 10 present the average density profiles of starless cores, prestellar core candidates, and protostellar cores, respectively. We normalized each respective core type's column density profile before averaging. The truncated radius R_t decreases as dense cores evolve from starless to protostellar. The size of the central flat region (a) is significantly larger in the starless cores (the mean value of a is 0.48 pc for starless cores), but is comparable between the prestellar candidates and protostellar cores (values of a for both prestellar candidates and protostellar cores are 0.26 pc). This indicates that the starless cores are less peaked than prestellar core candidates or protostellar cores.

Figure 11 presents R_d, a_d, and n_c. The upper panel of Figure 11 presents the results from fits to the column density profile for each core. The red, green, and blue dots are protostellar cores, prestellar core candidates, and starless cores, respectively. The bottom panel shows the values from fits to averaged protostellar cores, prestellar core candidates, and starless cores. According to the statistics of the fitting results (see Table 10), the denser the cores are, the smaller the values of R_d and a are. In other words, the dense cores will show steeper density structures when they evolve from starless cores to prestellar or protostellar cores.

4.3. CO Depletion

Gaseous CO molecules can freeze out onto grain surfaces in cold and dense regions, and the CO molecules can return to the

Table 10
Statistics of Parameters

Classification		N_{H_2} (*Herschel*) (10^{22} cm^{-2})	N_{H_2} (PMO) (10^{22} cm^{-2})	T_d (K)	V_{lsr} (km s^{-1})	σ_{th} (km s^{-1})	σ_{NT} (^{13}CO) (km s^{-1})	σ_{3D} (km s^{-1})	σ_{NT} (C^{18}O) (km s^{-1})	Mach Number	R(*Herschel*) (pc)
all cores	Mean	1.10	0.40	12.1	6.57	0.19	0.51	0.94	0.38	2.08	0.12
	Max	2.46	0.68	13.8	7.78	0.21	0.73	1.32	0.71	3.83	0.31
	Min	0.36	0.13	11.1	5.37	0.16	0.36	0.70	0.19	1.00	0.044
	Median	1.05	0.38	12.0	6.53	0.20	0.51	0.95	0.36	1.94	0.11
starless cores	Mean	0.86	0.38	12.1	6.48	0.19	0.50	0.94	0.36	1.99	0.15
	Max	1.40	0.68	13.1	7.78	0.21	0.73	1.32	0.56	3.04	0.31
	Min	0.36	0.13	11.5	5.37	0.16	0.36	0.71	0.22	1.07	0.096
	Median	0.86	0.38	12.1	6.49	0.18	0.49	0.91	0.34	1.82	0.12
prestellar candidates	Mean	1.47	0.43	11.6	6.76	0.19	0.54	1.00	0.42	2.21	0.099
	Max	2.46	0.68	13.2	7.19	0.21	0.67	1.21	0.62	3.41	0.14
	Min	1.05	0.35	11.1	5.89	0.18	0.43	0.81	0.23	1.11	0.061
	Median	1.29	0.38	11.1	6.97	0.19	0.52	0.96	0.41	2.26	0.098
protostellar cores	Mean	1.22	0.39	12.4	6.56	0.19	0.47	0.87	0.40	2.14	0.090
	Max	2.12	0.47	13.8	7.10	0.19	0.64	1.16	0.71	3.83	0.22
	Min	0.78	0.25	11.3	5.97	0.18	0.36	0.70	0.19	1.00	0.044
	Median	1.13	0.39	12.2	6.49	0.19	0.43	0.84	0.37	1.99	0.065

Classification		M_{core} ($M_\odot$)	M_{vir} ($M_\odot$)	α	Jeans Length (pc)	n_{H_2} (10^4 cm^{-3})	$N_{C^{18}O}$ (10^{14} cm^{-2})	C^{18}O abundance (10^{-7})	f_D	a_d (pc)	N_c (10^{22} cm^{-2})	n_c (10^4 cm^{-3})
all cores	Mean	13.76	21.43	3.49	0.216	2.88	12.86	1.64	1.56	0.038	1.78	6.63
	Max	59.83	74.28	17.46	0.440	7.87	22.89	2.87	6.59	0.089	4.51	18.11
	Min	1.21	3.60	0.25	0.111	0.57	1.58	0.66	1.00	0.014	0.66	1.31
	Median	7.75	17.55	2.28	0.206	2.33	12.52	1.65	2.24	0.030	1.61	5.01
starless cores	Mean	15.90	24.46	2.73	0.268	1.48	13.27	1.57	1.86	0.048	1.27	3.50
	Max	59.83	74.28	7.09	0.440	2.53	22.89	2.87	6.59	0.089	2.10	6.76
	Min	3.62	6.48	0.45	0.189	0.57	1.58	0.44	1.00	0.021	0.66	1.31
	Median	7.73	23.49	2.27	0.240	1.57	14.58	1.61	1.74	0.047	1.20	3.11
prestellar candidates	Mean	12.89	21.04	2.64	0.158	3.96	12.03	0.81	3.66	0.026	2.50	10.33
	Max	37.79	50.51	4.97	0.202	5.01	22.32	0.99	4.70	0.039	4.51	17.74
	Min	3.22	9.49	0.25	0.128	2.53	0.76	0.61	2.91	0.023	1.80	6.94
	Median	8.63	14.33	2.45	0.158	4.43	10.82	0.84	3.41	0.025	1.10	9.76
protostellar cores	Mean	10.79	16.64	5.30	0.167	4.49	12.73	1.12	3.07	0.026	2.34	10.74
	Max	36.43	35.66	17.46	0.244	7.87	19.63	1.64	5.97	0.042	3.79	18.11
	Min	1.21	3.60	0.36	0.111	1.22	0.63	0.48	1.75	0.014	1.37	4.35
	Median	4.50	16.68	2.32	0.162	4.12	12.82	1.28	2.30	0.023	2.27	10.91

Note. The statistics of the main parameters for our analysis results. For all parameters, we represent the mean, maximum, minimum, and median values for all cores, starless cores, prestellar candidates, and protostellar cores, respectively. However, we have not included the SCUBA-2 data in this statistic, because only parts of the dense cores have been detected by SCUBA-2.

gas phase as the temperature rises due to heating from protostars (Bergin & Langer 1997; Charnley 1997; Zhang et al. 2017).

Since C^{18}O emission is generally optically thin, it is a more reliable tracer for CO depletion than ^{12}CO or ^{13}CO. We calculate the core-averaged C^{18}O abundance of each dense core as follows:

$$X = \frac{N_{C^{18}O}}{N_{H_2}(Herschel)}, \quad (15)$$

where N_{H_2} is the core's *Herschel*-derived column density of H_2 (listed in Table 3), and $N_{C^{18}O}$ is the C^{18}O column density. It should be noted that the G166.99-15.34-H1 and G167.23-15.32-H1 are located outside of the densest parts of the filament, and with exceptionally low C^{18}O abundances. The low C^{18}O abundance in these two cores may be attributed to the fact that they are less shielded from interstellar UV radiation and the CO molecules inside them are more easily dissociated. Thus, the C^{18}O abundances of these two dense cores are very low, and they were excluded from fitting. In

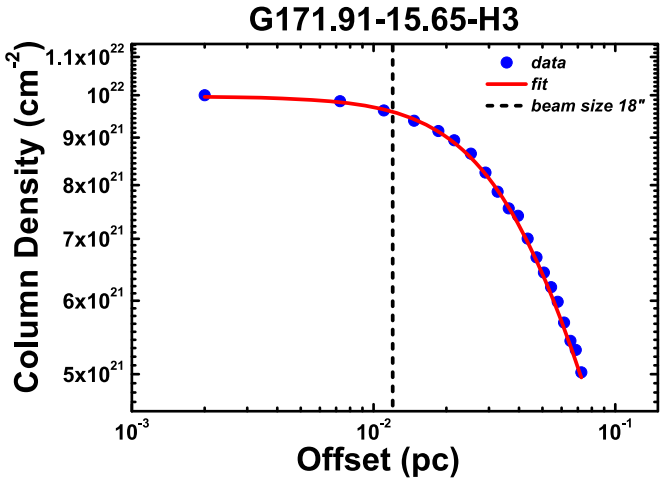

Figure 9. Column density profiles of the dense core for G171.91-15.65-H3. The red solid line represents the corresponding fit. The fitting results of N_c, R, and a are listed in Table 9. The flat central region and power-law decline can be seen in the figure. Due to its small size, we cannot obtain average column density distributions accurately for G170.26-16.02-H1 and G171.91-16.15-H1, and the flat region a of G171.91-15.65-H1 is smaller than the beam size. Therefore, we only present the column density profile for G171.91-15.65-H3 in this section. The images for other sources are shown in the figure set.

(The complete figure set (27 images) is available.)

Figure 12, the red diamonds, green squares, and blue dots represent the protostellar cores, prestellar core candidates, and starless cores, respectively. $C^{18}O$ abundance is clearly anti-correlated with the column density, which also indicates that the CO depletion becomes more prevalent in denser cores.

In this work, we simply define a relative CO depletion factor (f_D) of dense cores as follows:

$$f_D = \frac{X_{max}}{X_{core}}, \quad (16)$$

where X_{max} is the maximum $C^{18}O$ abundance in all the L1495 dense cores, and X_{core} is the $C^{18}O$ abundance of a dense core. The CO depletion factors (f_D) range from 1 to 6.6($\pm$1.8), and for each core these parameters are listed in Table 7. Please note that the CO depletion factors derived here should be treated as lower limits because we used core-averaged values. The CO depletion could be even more severe toward the core center.

Figure 13 presents f_D and the central volume densities (n_c) of the L1495 dense cores. There is a clear positive correlation between f_D and n_c, indicating that CO depletion is more significant in denser cores. The starless cores are shown in the bottom left corner of Figure 13, thus these cores have the smallest CO depletion factors. CO depletion in prestellar candidates and protostellar cores is more significant than that in starless cores. The mean depletion factors of starless cores, prestellar core candidates, and protostellar cores are 1.9($\pm$0.7), 3.7($\pm$0.7), and 3.1($\pm$1.5), respectively. The prestellar candidates and protostellar cores are mixed with each other in Figures 12 and 13, indicating that the protostellar cores in L1495 are still at the earliest phases of star formation and thus have as a high degree of CO depletion as prestellar core candidates.

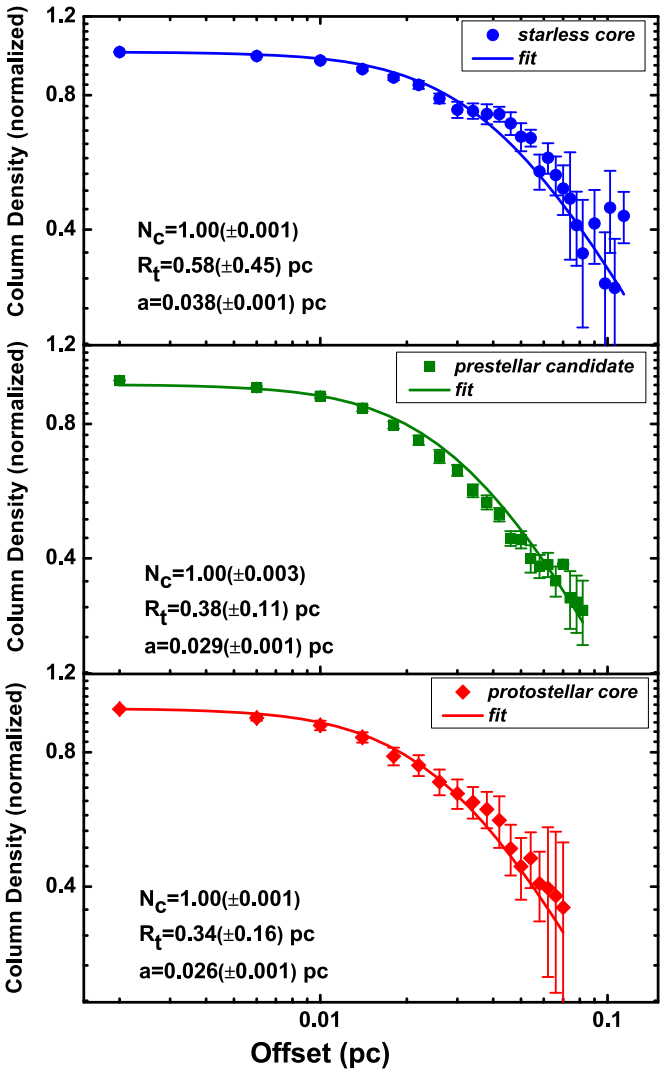

Figure 10. Average column density profile of starless cores (upper panel), prestellar core candidates (middle panel), and protostellar cores (bottom panel), respectively. The fitting results of N_c, R_t, and a are shown in each panel.

5. Summary

To better understand the properties of PGCCs and dense cores in L1495 cloud, we have studied 16 dense clumps in the L1495 cloud with data from *Herschel*, JCMT/SCUBA-2, and the PMO 13.7 m telescope. The main findings of this work are as follows:

1. In the L1495 region of Taurus, we identified 30 dense cores in 16 PGCCs. The majority of Planck clumps have *Herschel* cores, often multiple, but only a subset of the *Herschel* cores have corresponding SCUBA-2 condensations. Based on SCUBA-2 and *Herschel* 70 μm data, we have classified these 30 dense cores into three types: 15 are starless cores (i.e., with neither SCUBA-2 nor *Herschel* 70 μm emission), 6 are prestellar core candidates (i.e., with SCUBA-2 emission but without *Herschel* 70 μm emission) and 9 are protostellar cores (i.e., with *Herschel* 70 μm emission). Our findings suggest that not all PGCCs contain prestellar objects. In general, however, the dense cores in PGCCs are usually at early evolutionary stages.

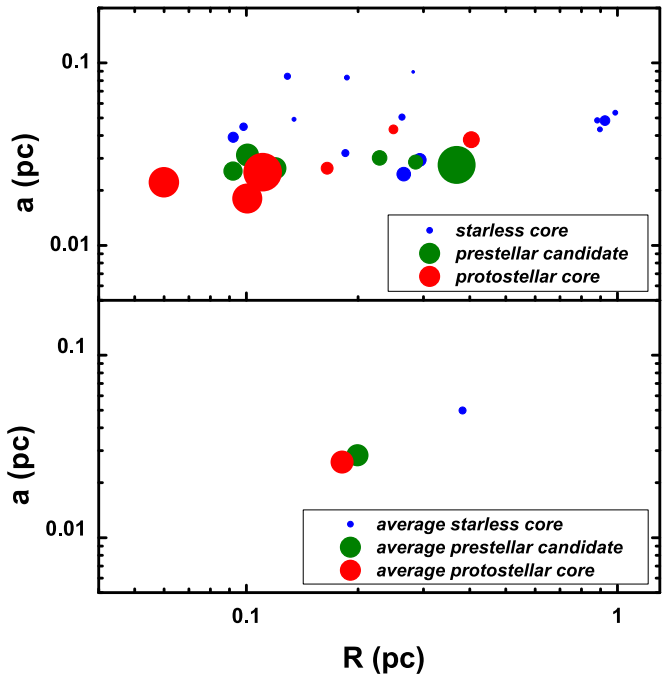

Figure 11. Top: the relationships between R_d, a_d, and n_c for L1495 dense cores. The x axis represents the radius R_d, and the y axis represents the flat region a_d. The relative central volume densities n_c ranging from 1.3×10^4 to 1.8×10^5 cm^{-3} are shown by the sizes of the data points. Bottom: the relationships between R_d, a_d, and n_c of averaged protostellar cores, prestellar core candidates, and starless cores. In both panels, the red, green, and blue dots represent protostellar cores, prestellar core candidates, and starless cores, respectively.

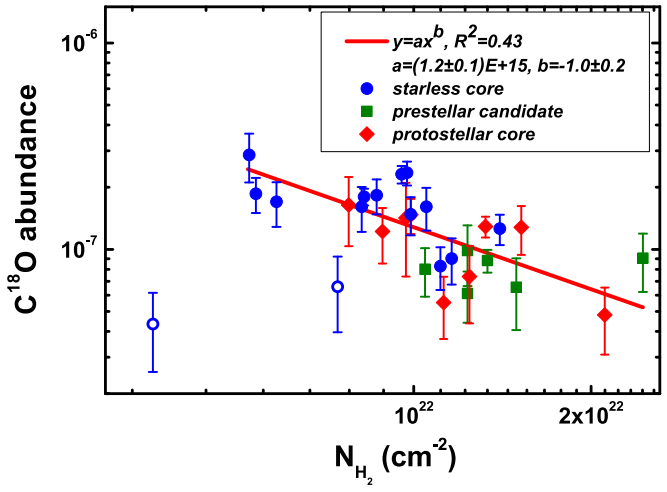

Figure 12. Correlation of $C^{18}O$ abundance and *Herschel* N_{H_2}. The red line is a power-law fit. The red diamonds, green squares, and blue dots represent the protostellar cores, prestellar core candidates, and starless cores, respectively. The blue circles represent G166.99-15.34-H1 and G167.23-15.32-H1, and they are located outside of the densest parts of the filament. Thus, we excluded them from fitting. The function and coefficients of models are presented in the upper-right corner of the image. A potential anti-correlation is found in the figure.

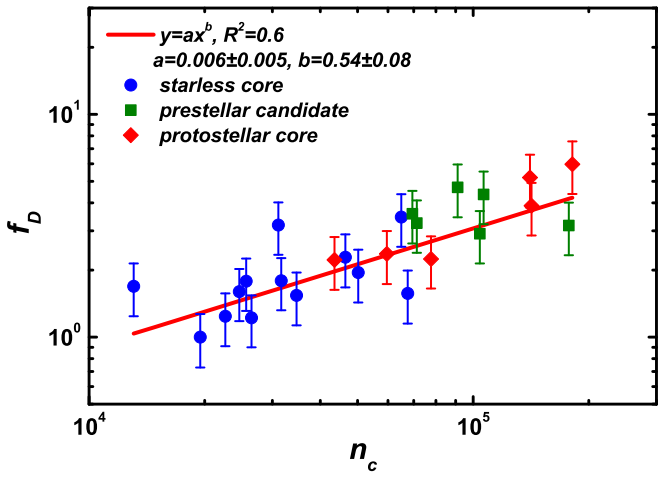

Figure 13. Correlation of relative depletion factors (f_D) and the central volume densities n_c (*Herschel*). The red line is a power-law fit, and blue dots, green squares, and red diamonds represent starless cores, prestellar core candidates, and protostellar cores, respectively.

2. Based on *Herschel* data, the mean volume densities of the starless cores, prestellar core candidates and protostellar cores are $1.0(\pm0.4) \times 10^4$ cm^{-3} cm^{-3}, $2.5(\pm0.6) \times 10^4$ cm^{-3}, and $2.7(\pm1.0) \times 10^4$, respectively. The mean dust temperatures of the starless cores, prestellar core candidates and protostellar cores are 12.1($\pm$0.4) K, 11.6 ($\pm$0.8) K, and 12.4($\pm$0.7) K, respectively. On average, prestellar core candidates have slightly lower dust temperature and higher density than starless cores. The 9 protostellar cores appear to still be at the earliest protostellar evolutionary phases and the newly formed protostars have not significantly heated their envelopes.
3. Non-thermal and thermal velocity dispersions have been derived from the PMO data. In all 30 dense cores, the Mach numbers are all larger than 1, with an average value of 2.1($\pm$0.8). Hence, the turbulence in the L1495 dense cores is supersonic, and all 30 dense cores may be turbulence-dominated.
4. The virial masses (M_{vir}) derived from the $C^{18}O$ data range from 3.6($\pm$0.7) $M_\odot$ to 74.3($\pm$7.6) $M_\odot$. The virial parameters (α) range from 0.3($\pm$0.1) to 17.5($\pm$7.3). Fourteen dense cores have virial parameters smaller than 2, and 18 dense cores have virial parameters larger than 2. The virial parameter and core mass follow the power-law trend, $\alpha = \alpha_{min} \cdot (M_{core}/M_{max})^{h_\alpha}$, with $h_\alpha = -0.74(\pm0.08)$.
5. The column density profiles of 28 dense cores have been derived from *Herschel* data. The central volume density (n_c), the size of the flat region (a), and the truncated radius (R_t) were obtained by fitting a column density profile. We found that the values of flat region size and truncated radius decrease as n_c increases. This indicates that dense cores shrink as they evolve from starless cores to protostellar cores (Ward-Thompson et al. 1994).
6. The $C^{18}O$ abundances are used to investigate the CO depletion degree in three types of dense cores. The mean $C^{18}O$ abundances of protostellar cores, prestellar core candidates, and starless cores are $1.12(\pm0.48) \times 10^{-7}$, $8.07(\pm1.34) \times 10^{-8}$ and $1.57(\pm0.65) \times 10^{-7}$, respectively. This variation means that CO depletion in prestellar core candidates is most significant. The core-averaged CO depletion factors (f_D) range from 1 to 6.6 ($\pm$1.8). Our results support the idea that the $C^{18}O$ abundance can be used as an evolutionary tracer for molecular cloud cores, as suggested by Caselli et al. (1999), Di Francesco et al. (2007), and Liu et al. (2013).

S.-L. Qin is supported by the National Key R&D Program of China (NO. 2017YFA0402701), by the Joint Research Fund in Astronomy (U1631237) under cooperative agreement between the National Natural Science Foundation of China (NSFC) and the Chinese Academy of Sciences (CAS), and by the Top Talents Program of Yunnan Province (2015HA030). Tie Liu is supported by a KASI fellowship and a EACOA fellowship. Ke Wang is supported by grant WA3628-1/1 of the German Research Foundation (DFG) through the priority program 1573 ("Physics of the Interstellar Medium"). This research was partly supported by the OTKA grant NN-111016. We thank Michel Fich, Mika Juvela, Jan Wouterloot, Archana Soam, M. R. Cunningham, Chang Won Lee, Paul F. Goldsmith, A. Rivera-Ingraham, Jinghua Yuan, Pak Shing Li, Johanna Malinen, George J. Bendo, Hong-Li Liu, Miju Kang, Neal J. Evans II, Patricio Sanhueza, Edith Falgarone, Glenn J. White, Izaskun Jimenez-Serra, You-Hua Chu, Yao-Lun Yang, JinHua He, and Hauyu Baobab Liu for helpful discussions and comments. The James Clerk Maxwell Telescope is operated by the East Asian Observatory on behalf of The National Astronomical Observatory of Japan, Academia Sinica Institute of Astronomy and Astrophysics, the Korea Astronomy and Space Science Institute, the National Astronomical Observatories of China and the Chinese Academy of Sciences (grant No. XDB09000000), with additional funding support from the Science and Technology Facilities Council of the United Kingdom and participating universities in the United Kingdom and Canada. Additional funds for the construction of SCUBA-2 were provided by the Canada Foundation for Innovation. This research has made use of data from the Herschel Gould Belt survey (HGBS) project (http://gouldbelt-herschel.cea.fr). The HGBS is a Herschel Key Programme jointly carried out by SPIRE Specialist Astronomy Group 3 (SAG 3), scientists of several institutes in the PACS Consortium (CEA Saclay, INAF-IFSI Rome and INAF-Arcetri, KU Leuven, MPIA Heidelberg), and scientists of the *Herschel* Science Center (HSC).

ORCID iDs

Mengyao Tang https://orcid.org/0000-0001-9160-2944
Tie Liu https://orcid.org/0000-0002-5286-2564
Sheng-Li Qin https://orcid.org/0000-0003-2302-0613
Kee-Tae Kim https://orcid.org/0000-0003-2412-7092
Yuefang Wu https://orcid.org/0000-0002-5076-7520
Ken'ichi Tatematsu https://orcid.org/0000-0002-8149-8546
Ke Wang https://orcid.org/0000-0002-7237-3856
Harriet Parsons https://orcid.org/0000-0002-6327-3423
Patrick M. Koch https://orcid.org/0000-0003-2777-5861
Patricio Sanhueza https://orcid.org/0000-0002-7125-7685
D. Ward-Thompson https://orcid.org/0000-0003-1140-2761
James Di Francesco https://orcid.org/0000-0002-9289-2450
Chuan-Peng Zhang https://orcid.org/0000-0002-4428-3183

References

André, P., Di Francesco, J., Ward-Thompson, D., et al. 2014, in Protostars and Planets VI, ed. H. Beuther et al. (Tucson, AZ: Univ. Arizona Press), 27
André, Ph., Men'shchikov, A., Bontemps, S., et al. 2010, A&A, 518, L102
Bergin, E. A., & Langer, W. D. 1997, ApJ, 486, 316
Bertoldi, F., & Mckee, C. F. 1992, ApJ, 395, 140
Bintley, D., Holland, W. S., MacIntosh, M. J., et al. 2014, Proc. SPIE, 9153, 915303
Buckle, J. V., Drabek-Maunder, E., Greaves, J., et al. 2015, MNRAS, 449, 2472
Caselli, P. 2011, in IAU Symp. 280, The Molecular Universe, ed. J. Cernicharo & R. Bachiller (Cambridge: Cambridge Univ. Press), 19
Caselli, P., Walmsley, C. M., Tafalla, M., Dore, L., & Myers, P. C. 1999, ApJL, 523, L165
Chackerian, C., & Tipping, R. H. 1983, JMoSp, 99, 431
Chapin, E., Gibb, A. G., Jenness, T., et al. 2013, StaUN, 258
Charnley, S. B. 1997, MNRAS, 291, 455
Currie, M. J., Berry, D. S., Jenness, T., et al. 2014, in ASP Conf. Ser. 485, adass XXIII, ed. N. Manset & P. Forshay (San Francisco, CA: ASP), 391
Dapp, W. B., & Basu, Shantanu. 2009, MNRAS, 395, 1092D
Dempsey, J. T., Friberg, P., Jenness, T., et al. 2013, MNRAS, 430, 2534D
Di Francesco, J., Evans, N. J., II, Caselli, P., et al. 2007, in Protostars and Planets V, ed. B. Reipurth, D. Jewitt, & K. Keil (Tucson, AZ: Univ. Arizona Press), 17
Elias, J. H. 1987, ApJ, 224, 857
Fehér, O., Juvela, M., Lunttila, T., et al. 2017, A&A, 606, A102
Friesen, R. K., Bourke, T. L., Di Francesco, J., Gutermuth, R., & Myers, P. C. 2016, ApJ, 833, 204
Garden, R. P., Hayashi, M., Hasegawa, T., Gatley, I., & Kaifu, N. 1991, ApJ, 374, 540
Giannetti, A., Wyrowski, F., Csengeri, T., et al. 2014, A&A, 570, A65
Hacar, A., Tafalla, M., Kauffmann, J., & Kovács, A. 2013, A&A, 554, A55
Hawkins, I., & Jura, M. 1987, ApJ, 317, 926
Hildebrand, R. H. 1983, QJRAS, 24, 267
Holland, W. S., Bintley, D., Chapin, E. L., et al. 2013, MNRAS, 430, 2513
Jeans, J. H. 1928, Astronomy and Cosmogony (Cambridge: Cambridge Univ. Press)
Juvela, M., He, J., Pattle, K., et al. 2017, A&A, in press (arXiv:1711.09425)
Kauffmann, J., Bertoldi, F., Bourke, T. L., Evens, N. J., II, & Lee, C. W. 2008, A&A, 487, 993
Kauffmann, J., Pillai, T., & Goldsmith, P. F. 2013, ApJ, 779, 185
Kenyon, S. J., Dobrzycka, D., & Hartmann, L. 1994, AJ, 108, 1872
Kim, J., Lee, J.-E., Liu, T., et al. 2017, ApJS, 231, 9
Kirk, J. M., Ward-Thompson, D., Palmeirim, P., et al. 2013, MNRAS, 432, 1424K
Könyves, V., André, Ph., Men'shchikov, A., et al. 2015, A&A, 584, A91
Liu, T., Kim, K.-T., Juvela, M., et al. 2018, ApJS, 234, 28
Liu, T., Wu, Y., & Mardones, D. 2014, PKAS, 30, 79L
Liu, T., Wu, Y., & Zhang, H. 2012, ApJS, 202, 4
Liu, T., Wu, Y., & Zhang, H. 2013, ApJL, 775, L2
Liu, T., Zhang, Q., Kim, K.-T., et al. 2016, ApJS, 222, 7
Loinard, L., Torres, R. M., Mioduszewski, A. J., & Rodríguez, L. F. 2008, RMxAC, 34, 14
Loren, R. B. 1989, ApJ, 338, 925
Mac Low, M.-M., & Klessen, R. S. 2004, RvMP, 76, 125
MacLaren, I., Richardon, K. M., & Wolfendale, A. W. 1988, ApJ, 333, 821
Mairs, S., Johnstone, D., Kirk, H., et al. 2015, MNRAS, 454, 2557
Marsh, K. A., Griffin, M. J., Palmeirim, P., et al. 2014, MNRAS, 439, 3683M
Marsh, K. A., Kirk, J. M., André, Ph., et al. 2016, MNRAS, 459, 342
Meng, F., Wu, Y., & Liu, T. 2013, ApJS, 209, 37
Ohashi, S., Sanhueza, P., Chen, H.-R. V., et al. 2016, ApJ, 833, 209
Onishi, T., Mizuno, A., Kawamura, A, Ogawa, H., & Fukui, Y. 1996, ApJ, 465, 815
Onishi, T., Mizuno, A., Kawamura, A., Tachihara, K., & Fukui, Y. 2002, ApJ, 575, 950
Pattle, K., Ward-Thompson, D., Kirk, J. M., et al. 2015, MNRAS, 450, 1094
Penzias, A. A. 1980, Sci, 208, 663
Pilbratt, G. L., Riedinger, J. R., Passvogel, T., et al. 2010, A&A, 518, L1
Planck Collaboration, Ade, P. A. R., Aghanim, N., et al. 2011, A&A, 536, 23
Planck Collaboration, Ade, P. A. R., Aghanim, N., et al. 2016, A&A, 594, A28
Sanhueza, P., Jackson, J. M., Zhang, Q., et al. 2017, ApJ, 841, 97
Sault, R. J., Teuben, P. J., & Wright, M. C. 1995, in ASP Conf. Ser. 77, adass IV, ed. R. A. Shaw, H. E. Payne, & J. J. E. Hayes (San Francisco, CA: ASP), 433
Schmalzl, M., Kainulainen, J., Quanz, S. P., et al. 2010, ApJ, 725, 1327
Seo, Y. M., Shirley, Y. L., Goldsmith, P., et al. 2015, ApJ, 805, 185S
Shan, W., Yang, Y., Shi, S., et al. 2012, ITTST, 2, 593
Straizys, V., & Meistas, E. 1980, AcA, 30, 541
Tachihara, K., Mizuno, A., & Fukui, Y. 2000, ApJ, 528, 817
Tatematsu, K., Liu, T., Ohashi, S., et al. 2017, ApJS, 228, 12
Torres, R. M., Loinard, L., Mioduszewski, A. J., et al. 2012, ApJ, 747, 18T

Tóth, L. V., Marton, G., Zahorecz, S., et al. 2014, PASJ, 66, 17
Tóth, L. V., Zahorecz, S., Marton, G., et al. 2017, in IAU Symp. 316, Formation, Evolution, and Survival of Massive Star Clusters, ed. C. Charbonnel & A. Nota (Cambridge: Cambridge Univ. Press), 133
Tóth, L. V., Zahorecz, S., Marton, G., et al. 2016, in IAU Symp. From Interstellar Clouds to Star-forming Galaxies, ed. P. Jablonka, P. André, & F. van der Tak (Cambirdge: Cambridge Univ. Press), E75
Van der Tak, F. F. S., Black, J. H., Schöier, F. L., Jansen, D. J., & van Dishoeck, E. F. 2007, A&A, 468, 627
Ward-Thompson, D., Di Francesco, J., Hatchell, J., et al. 2007, PASP, 119, 855
Ward-Thompson, D., Pattle, K., Kirk, J. M., et al. 2016, MNRAS, 463, 1008
Ward-Thompson, D., Scott, P. E., Hills, R. E., & André, P. 1994, MNRAS, 268, 276
Wu, Y., Liu, T., Meng, F., et al. 2012, ApJ, 756, 76
Yuan, J., Wu, Y., Liu, T., et al. 2016, ApJ, 820, 37
Zahorecz, S., Jimenez-Serra, I., Wang, K., et al. 2016, A&A, 591, A105
Zhang, C.-P., Yuan, J.-H., Li, G.-X., Zhou, J.-J., & Wang, J.-J. 2017, A&A, 598, A76
Zhang, Q., Wang, K., Lu, X., & Jiménez-Serra, I. 2015, ApJ, 804, 141
Zhang, T., Wu, Y., Liu, T., et al. 2016, ApJS, 224, 43